An advanced head-to-tail mouse embryo model with hypoxia-mediated neural patterning

Anastasios Balaskas[1,2], Isabelle Kraus[1,3], Hatice Ö. Özgüldez[1], Persia Akbari Omgba[1,4], René Buschow[1], Adriano Bolondi[1], Idan Berlad[5], Jacob H. Hanna[5], Helene Kretzmer[1,3], Aydan Bulut-Karslioğlu[1, §]

[1] Max Planck Institute for Molecular Genetics, 14195 Berlin, Germany
[2]Institute of Chemistry and Biochemistry, Department of Chemistry, Biology and Pharmacy, Freie Universität Berlin, 14195 Berlin, Germany
[3] Hasso-Plattner-Institute, 14482 Potsdam, Germany
[4] Department of Mathematics and Computer Science, Freie Universität Berlin, 14195 Berlin, Germany
[5] Department of Molecular Genetics, Weizmann Institute of Science, 76100 Rehovot, Israel
[§] Correspondence: Aydan Bulut-Karslioglu Aydan.karslioglu@molgen.mpg.de

SUMMARY

The developing mammalian embryo is guided by the continuously changing signals that it receives from maternal tissues and its microenvironment. The dynamic cell-cell and cell-environment interactions that together shape the embryo largely remained unexplorable until the advance of stem cell-based embryo models. These revealed the self-organizing properties of cells in response to endogenous and exogenous cues. Among the latter, restricted oxygen (hypoxia) emerged as a critical microenvironmental regulator that influences cell type diversification in multicellular systems. Here, by combining Hypoxia and an Antero-Posterior assembly strategy, we developed an ESC-based head-to-tail model of mouse embryogenesis called HAP-gastruloids. HAP-gastruloids contain stage-appropriate anterior brain-like tissues as well as spinal cord, somites, and gut endoderm. We show that timed hypoxia boosts anterior neural cell identities and their patterning through HIF1a and in part by modulating TGFβ superfamily activity. These results reveal a key beneficial role of hypoxia in early development and offer a unique system to investigate antero-posterior phenotypes for basic discovery and translation.

INTRODUCTION

The uterine habitat of the mammalian embryo nourishes, shapes, and guides the developing cells. Gas and nutrient exchange through the placenta is a vital part of mammalian development, yet, the earliest and most elemental stages of development take place before the placenta is formed and becomes fully functional. One such stage is gastrulation, during which the mammalian body plan is laid out, and the founding cells of all tissues are specified and initially localized. Over four decades of developmental biology research identified key signaling events that lay out the mammalian body plan[1], yet, the investigation of how the uterine microenvironment contributes to these complex and concurrent events is an emergent question. Specifically, how the presumably low-oxygen (hypoxic) environment resulting from the lack of developed vasculature and a functioning placenta impacts the complexity of the gastrulating embryo is poorly understood[2-4].

In the recent decade, various 2D/3D stem cell-based in vitro models of the developing embryo have been developed. The 3D models in particular revealed the remarkable self-organizing events in cellular aggregates, often

yielding structures that closely recapitulate embryonic events under minimal guidance. The extent to which these structures present complex embryonic tissues along the three axes of symmetry depends largely on the complexity of the initial group of cells. The so-called 'integrated' models are generated using embryonic and extraembryonic stem cells and model the entire mammalian conceptus, including extra-embryonic tissues[5], while 'non-integrated' models, generated using embryonic stem cells (ESCs), robustly recapitulate specific aspects of embryonic development[6-24]. Among the latter, gastruloids represent posterior gastrulation events and have been widely adopted to investigate cellular decision-making and self-organization properties[13]. However, a major limitation of gastruloids and gastruloid-derivatives models[9,12,25,26] is the lack of brain specification and insufficient representation of other anterior cell fates. An effort has been made to generate anterior tissues in gastruloids[27-29], however, a gap persists for the generation of sufficiently developed and morphologically organized structures with anterior tissues.

We have previously shown that the combined exposure of gastruloids to 2% oxygen (O_2) and the WNT activator Chiron increases the cellular complexity of conventional gastruloids, whereas exposure to 2% O_2 in the absence of Chiron allows the generation of brain-like tissues[30]. Additionally, timed and gradual exposure of embryos to low oxygen concentrations during ex utero mouse gastrulation results in higher survival of normally developed embryos compared to normoxia[31]. Deletion of the hypoxia-inducible factor 1a gene (*Hif1a*) in mice results in gestational deficiencies that go beyond the expected vascularization defects and extend into neural tube and forebrain formation[32]. Furthermore, within the rat neural lineage, different types of neurons can be generated under differing O_2 concentrations[2,33,34]. Together, oxygen appears to modulate cell fates in a concentration-dependent manner comparable to a developmental morphogen.

Leveraging these effects of oxygen concentration in the context of embryonic assembloids, here we show that hypoxia boosts the commitment to and patterning of anterior neural 'brain-like' cells along the Anterior-Posterior (A-P axis). Hypoxic A-P gastruloids present a robust and modular embryo model that illuminates the early organogenesis stages.

RESULTS

Hypoxic A-P (HAP) gastruloids recapitulate the anterior-posterior axis of the early organogenesis stage mouse embryo

To test the limits of cell type diversification via hypoxia in a self-organizing early embryonic differentiation system, we first used the gastruloid-like system called Trunk Like Structures (TLS)[9,12]. TLSs are formed from a single, transgene-free ESC aggregate over 120 hours. A transient pulse of the WNT agonist Chiron between 48-72h allows symmetry breaking and axial elongation. Addition of extracellular matrix in the form of matrigel in the last 24h enables the emergence of stage-appropriate morphological features such as the neural tube, somites, and occasionally, a gut tube (Figure S1A,D). TLSs, however, have highly variable morphology and entirely lack more anterior tissues such as the brain[35,36]. We first systematically tested the effect of hypoxia on TLS morphology and tissue composition by altering the duration and severity of hypoxia before and during TLS formation (Figure S1). Early and continuous exposure to 2% O_2 boosted gut endoderm formation but compromised the axial elongation and overall area, which was rescued when the structures were exposed to ambient oxygen in the last 24-48h (Figure S1A-D). These results suggested that early exposure to hypoxia enriches gut endoderm composition, whereas late exposure during elongation stages compromises morphology. Integrating early hypoxia exposure with late normoxia, with a gradual increase of oxygen levels in between, led to the formation of well-elongated structures. However, these structures exhibited short neural tubes and disorganized anterior regions (Figure

Figure 1 : HAP-gastruloids recapitulate the entire A-P axis at E8.75-E9.0

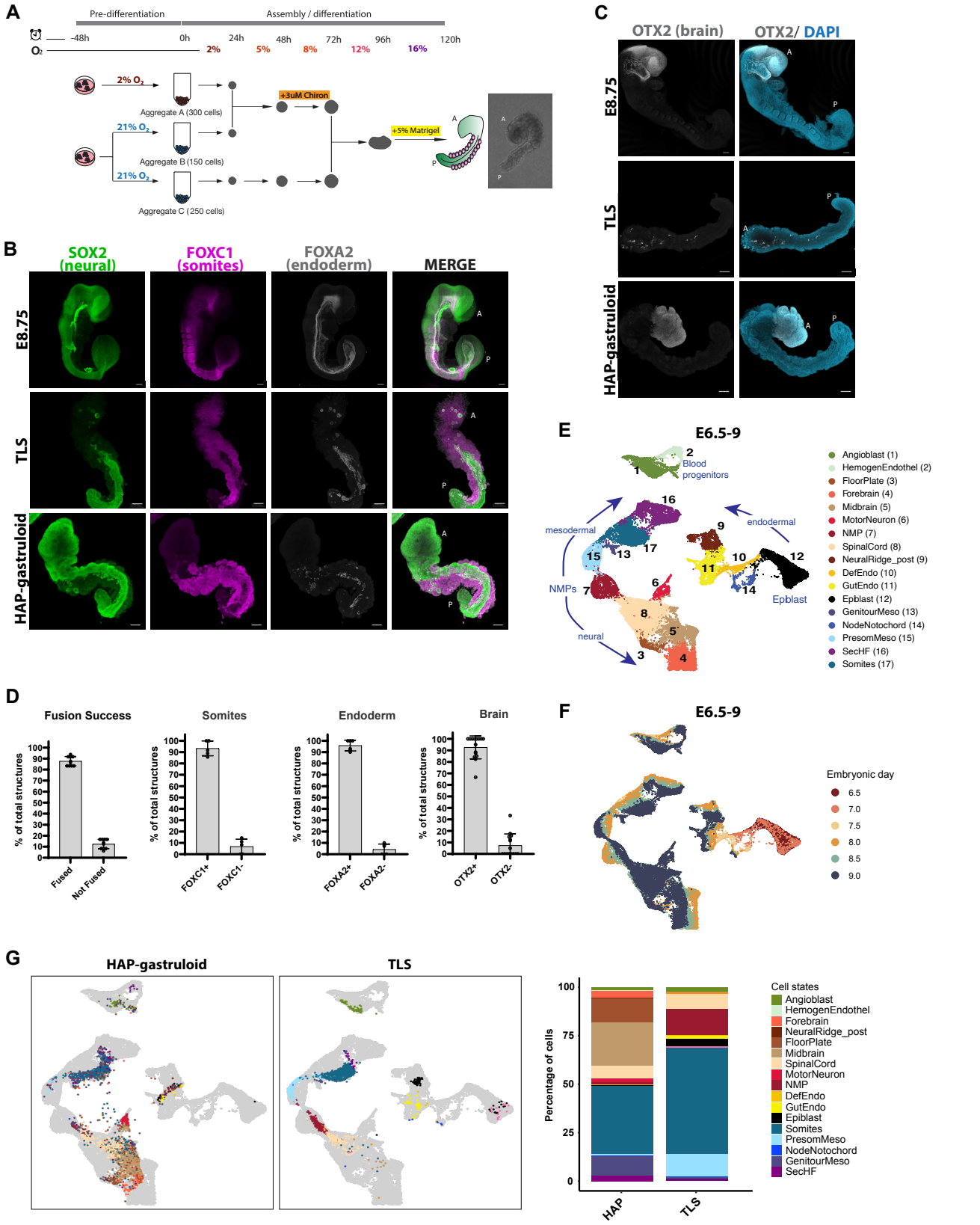

A. Schematic illustration of the experimental pipeline for HAP-gastruloid generation.
B. Immunofluorescence (IF) staining of E8.75 mouse embryo, TLS and HAP-gastruloid for neural marker SOX2, somitic marker FOXC1 and endoderm marker FOXA2. A: Anterior, P: Posterior. Scale bars, 100 µm.

C. IF staining of mouse embryo at E8.75, TLS and HAP-gastruloid for brain marker OTX2 and DAPI. A: Anterior, P: Posterior. Scale bars, 100 µm

D. Percentage of total structures per biological replicate showing fusion success, somite, endoderm and brain formation in HAP-gastruloid. Column heights show mean, and error bars indicate standard deviation. Each dot represents a different biological replicate. For fusion success 10 biological replicates were used (600 individual structures in total, 522 of which were successfully fused generating HAP-gastruloids). For somite formation 5 biological replicates were used (67 structures in total, 62 of which successfully formed somites). For endoderm formation 6 biological replicates were used (total number 64 individual structures, 61 of which successfully formed gut endoderm). For formation of the brain-like region, 15 biological replicates were used (228 structures, 207 of which successfully formed the brain-like region).
E. UMAP plot of mouse embryo reference scRNA-seq data stages between E6.5 to E9[45]. Colors represent different cell types. Cell types that are detected in HAP-gastruloids are shown. Arrows show lineage trajectories.
F. UMAP plot of mouse embryo reference scRNA-seq data showing stages between E6.5 to E9. The distinct developmental stages are colored as shown.
G. Left, UMAP plot of HAP- gastruloids and TLS generated from scRNA-seq data. Colors represent cell types. Right, stacked plots showing percentages of the indicated cell types per condition.
HemogenEndothel: Hemogenic endothelium, NeuralRidge_post: Posterior Neural Ridge, NMP: Neural Mesodermal Progenitor, DefEndo: Definitive Endoderm, GutEndo: Gut Endoderm, PresomMeso: Presomitic Mesoderm, GenitourMeso: Genitourinary mesoderm (Pronephron), SecHF: Secondary Heart Field

S1A-D). Additionally, none of these conditions generated structures that contained neural cells anterior to somites. We concluded that starting with a single aggregate is incompatible with recapitulating the entire A-P axis of the corresponding stage embryo.

The gastrulating mouse embryo creates a WNT gradient with high WNT activity at the posterior end, which is antagonized at the anterior end, allowing the generation of early brain cells. We reasoned that generating such a gradient *in vitro* may allow the formation of stage-appropriate cells along the entire A-P axis. To achieve this, we designed a new, assembly-based experimental approach. Assembly-based models (assembloids) successfully recapitulate the morphological and compositional complexity of other mammalian tissues, such as the cortical-motor and cortical-vascular tissues of the brain[37-44]. To generate a model with an inherent WNT gradient along the A-P axis, we assembled a Chiron-treated aggregate with a Chiron-free aggregate in 1:1 ratio (conditions XI and XII, Figure S2A-D). The two aggregates were put together at 72h, were completely fused by 96h into a single structure, which then elongated in the next 24h. All cells in this system experience gradually decreasing hypoxia during differentiation. Notably, A-P assembloids robustly formed somites (FOXC1), a posterior neural tube (SOX2) as well as an anterior neural domain characterized by the midbrain/ forebrain marker OTX2 (Figure S2B-C). Hypoxia pre-treatment before differentiation achieved a neural tube-adjacent gut endoderm tissue but compromised the continuity of the neural tube (Figure S2B-C,E-F). We concluded that robust endoderm is mostly incompatible with a continuous neural tube formation.

To overcome this limitation, we next devised a 3-aggregate A-P assembloid model (condition XIII, Figure S2A). In this model, hypoxic and normoxic ESC aggregates A and B are fused first, then treated with Chiron, and further assembled with Chiron-free cells in 1:1:1 ratio (Figure S2A). These triple assembloids formed a continuous neural tube (70% of structures), robust gut endoderm (37% with proper cavity, 48% with rosettes), and an anterior brain-like domain (85%) (Figure S2E-G). A further iteration of adjusting cell numbers was done to equalize the size of each aggregate (Figure S2D). The resulting hypoxic A-P assembly model (HAP-gastruloid from here on) contains bilateral somites and FOXA2+ endoderm cells surrounding a continuous neural tube that extends into an anterior neural domain expressing SOX2 and OTX2 in a similar pattern to the E8.75-E9.0 embryo (Figure 1A-D). These phenotypes were robustly reproduced (~75-80% of all structures) using two separate ESC lines (Figure 1B-D, S3A-B).

To get a more in-depth overview of the cell type composition of HAP-gastruloids, we performed single cell RNA-sequencing (scRNA-seq) analysis of these and TLS. We pooled 6-20 structures per condition and analyzed a total number of 6041 HAP-gastruloid cells and 3031 TLS cells. For cell type annotation we used an expanded scRNA-seq atlas of the embryonic stages E6.5-E-9 (Figure 1E-F, see S4A-B for gene markers of specific clusters)[45]. These analyses validated our previous stainings and showed that, in contrast to TLS, HAP-gastruloids forms forebrain- and midbrain-like anterior neural tissues as well as motor neuron progenitors and genitourinary mesoderm. Compared to TLS, HAP-gastruloids contain proportionally less presomitic and somitic mesoderm, which is in part explained by the proportional increase in anterior neural cells (Figure 1G). In addition, there is a notable decrease in neuro-mesodermal progenitors (NMPs), which may be due to their transient nature. In conclusion, HAP-gastruloids contain and spatially organize an expanded range of embryonic tissues along the entire A-P axis, revealing a capacity for anterior-posterior cross-talk and co-organization that results in a unified embryo-like structure.

Figure 2 : HAP-gastruloids show appropriate neural patterning along the A-P axis

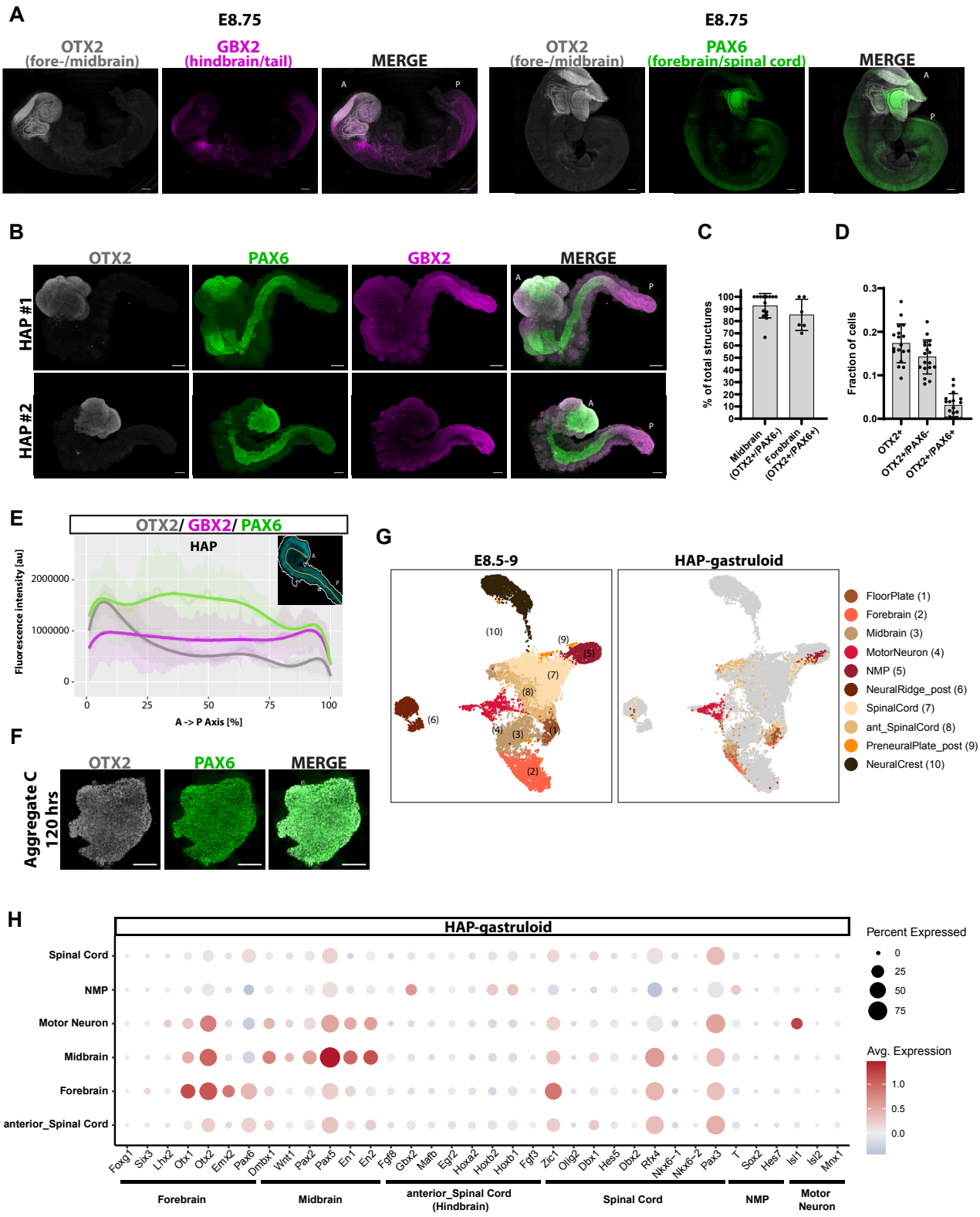

A. IF staining of E8.75 mouse embryo for the fore-/midbrain marker OTX2, hindbrain/NMP marker GBX2 and forebrain/spinal cord marker PAX6. A: Anterior, P: Posterior. Scale bars, 100 µm.

B. IF staining of HAP-gastruloids for fore-/midbrain marker OTX2, hindbrain/NMP marker GBX2 and forebrain/spinal cord marker PAX6. Scale bars, 100 µm.

C. Percentage of total structures per biological replicate showing midbrain and forebrain formation in HAP-gastruloids. Column heights show mean, and error bars indicate standard deviation. Each dot represents a different biological replicate. For midbrain formation 15 biological replicates were used (total number 228 individual structures, 207 of which successfully formed midbrain). For forebrain formation 6 biological replicates were used (total number 67 individual structures, 56 of which successfully formed forebrain).

D. Fraction of cells per structure expressing OTX2+, OTX2+/PAX6- (midbrain) and OTX2+/PAX6+ (forebrain) cells in HAP-gastruloids. Column heights show mean, and error bars indicate standard deviation. Each dot represents an individual structure. A total of 18 individual structures from 2 different biological replicates (9 structures/biological replicate) were used.

E. Localization of OTX2, GBX2 and PAX6 signals along the A-P axis of HAP-gastruloids. Lines show mean values from 10 individual structures. Small figure: line shows how the A-P axis was defined in structures.

F. IF staining of aggregate C (Chironless) at 120 hrs for fore-/midbrain marker OTX2 and forebrain/spinal cord marker PAX6. Scale bars, 100 µm.

G. Left, neural subclustering UMAP plot of mouse embryo reference scRNA-seq data stages between E6.5 to E9[45]. Colors represent cell types. Cell types detected in HAP-gastruloids are shown. Right, neural subclustering UMAP plot of HAP-gastruloids generated from scRNA-seq data.

H. Dot plot showing the expression of neural cell type specific marker genes in HAP-gastruloids. Dot size corresponds to the percentage of cells in the sample expressing the gene, color intensity reflects the scaled average expression level.

HAP-gastruloids show stage-appropriate neural patterning along the A-P axis

The most unique feature of HAP-gastruloids is the presence of a brain-like domain anterior to a continuous neural tube. The E8.5-9.0 mouse embryo contains primordial forebrain and midbrain regions that express PAX6 and OTX2 or only OTX2, respectively (Figure 2A). Posterior to these, PAX6 is also expressed in the spinal cord, while GBX2 is expressed in the anterior spinal cord (future hindbrain) and the tail. To test whether HAP-gastruloids successfully pattern the neural cells along the A-P axis and compartmentalize the brain-like region, we stained HAP-gastruloids for PAX6, OTX2, and GBX2 (Figure 2B, S5A-B). Over 90% of HAP-gastruloids contain an OTX2+ midbrain-like region and at least 70% contain a PAX6+ posterior forebrain domain depending on the cell line and replicate (Figure 2C-D, S5C-H). Single cell fluorescence intensity quantifications showed consistent enrichments of midbrain- and forebrain-like cells across structures (Figure 2D) and fluorescence intensity distribution along the A-P axis showed arrangement of forebrain, midbrain as well as the anterior and posterior spinal cord regions identical to the embryo (Figure 2E). This spatial patterning is a feature of the assembled HAP-gastruloids and is not observed in the stand-alone 'brain' aggregate (aggregate C), indicating that the posterior tissues influence patterning of the anterior ones (Figure 2F).

To benchmark the anterior neural tissues of HAP-gastruloids in more detail, we subclustered neural cell types detected in the scRNA-seq experiment and investigated marker expression (Figure 2G-H, S4B). This analysis revealed that HAP-gastruloids express midbrain markers Dmbx1 and Wnt1 as well as midbrain-hindbrain boundary markers Pax2, Pax5, En1 and En2. In addition, HAP-gastruloids express forebrain markers Pax6 and Emx2, but not markers of the most rostral forebrain such as Foxg1, Six3 and Lhx2. Hindbrain markers Gbx2 and Egr2 show mild expression in the anterior spinal cord cluster. Dorsal spinal cord markers Pax6, Zic1, Dbx1 and Pax3 are robustly expressed, while ventral spinal cord markers Olig2, Nkx6.1 and Nkx6.2 are not expressed. Together, the combined hypoxia-assembloid strategy yields robust neural patterning along the A-P axis, which is not seen in TLSs or stand-alone neural aggregates.

HAP-gastruloids develop synchronously and compose diverse tissues

Our results strongly suggest that the interactions between the different aggregates that give rise to HAP-gastruloids shape the final gene expression pattern and tissue organization. Thus, we next aimed to find out the specific contributions of each aggregate to the overall system. To achieve this, we used a SOX2::Venus and T::mCherry dual reporter ESC line[9] and formed HAP-gastruloids by labeling one aggregate at a time (Figure S6A). We observed that the Chiron-treated aggregates (A and B) both contributed to a range of posterior tissues. Yet, aggregate A mainly contributed to tissues surrounding the neural tube and somites (presumably endoderm, which cannot be visualized via this reporter), whereas aggregate B formed the neural tube (spinal cord) and somites. The Chiron-free aggregate C exclusively formed the brain-like anterior region and also contributed to anterior spinal cord. Occasionally, this contribution even extended to more posterior neural regions (Figure S6A). Thus, although the brain-like anterior end was generated only by aggregate C, interactions of cells originating from all three aggregates could be observed along a large portion of the A-P axis.

The aggregates develop independently until the moment of assembly. We next asked whether the tissues in the final HAP-gastruloid are synchronized with each other in terms of their developmental progress. Overall, HAP-gastruloids' final transcriptional state aligns with the E8.75-E9.0 embryo (Figure S6B-C). To assess the transcriptional stage of each cell in HAP-gastruloids, we performed a label transfer-based staging analysis[46] and plotted the predicted stage of each cell in each tissue (Figure S6D). This analysis revealed that most tissues, including

Figure 3 : Hypoxia boosts anterior neural fates

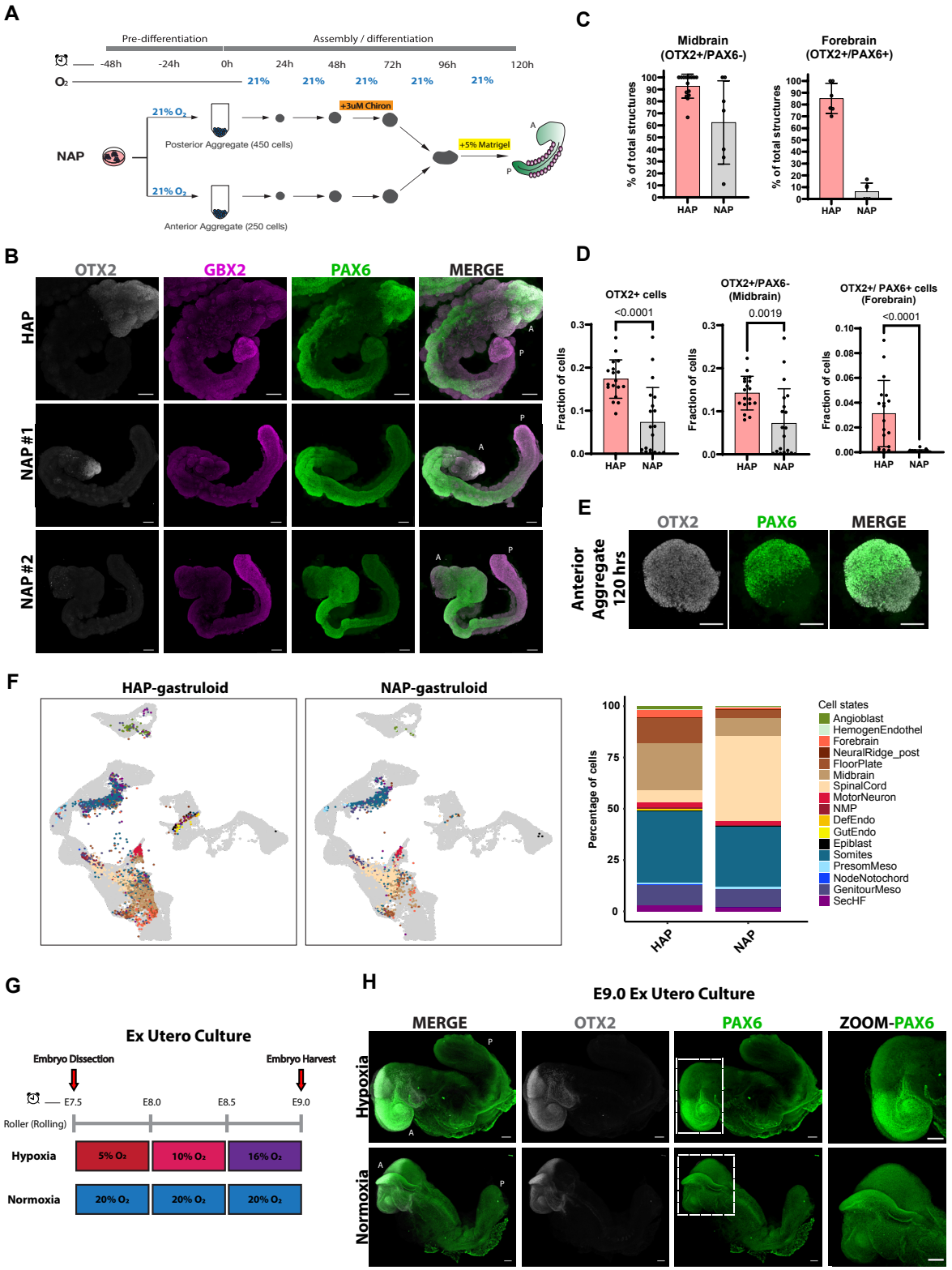

A. Schematic illustration of the experimental pipeline for NAP-gastruloid generation.

B. IF staining of HAP- and NAP-gastruloids for fore-/midbrain marker OTX2, hindbrain/NMP marker GBX2 and forebrain/spinal cord marker PAX6. A: Anterior, P: Posterior. Scale bars, 100 µm.

C. Percentage of total structures per biological replicate showing midbrain and forebrain formation in HAP- and NAP-gastruloids. Column heights show mean, and error bars indicate standard deviation. Each dot represents a different biological replicate. HAP-gastruloids: For midbrain formation 15 biological replicates were used (total number 228 individual structures, 207 of which successfully formed midbrain). For forebrain formation 6 biological replicates were used (total number 67 individual structures, 56 of which successfully formed forebrain). NAP-gastruloids: For midbrain formation 7 biological replicates were used (total number 73 individual structures, 44 of which successfully formed midbrain). For forebrain formation 6 biological replicates were used (total number 61 individual structures, 5 of which successfully formed forebrain)

D. Fraction of cells per structure expressing OTX2+, OTX2+/PAX6- (midbrain) and OTX2+/PAX6+ (forebrain) cells in HAP- and NAP-gastruloids. Column height and error bars indicate mean and standard deviation. Each dot represents an individual structure. HAP-gastruloids: a total of 18 individual structures from 2 different biological replicates (9 structures/biological replicate) were used. NAP-gastruloids: a total of 20 individual structures from 2 different biological replicates (10 structures/biological replicate) were used. Statistical test is unpaired two-tailed t test.

E. IF staining of NAP-gastruloid anterior aggregate (Chironless) at 120 hrs for fore-/midbrain marker OTX2 and forebrain/spinal cord marker PAX6. Scale bars, 100 µm.

F. Left, UMAP plot of HAP- and NAP-gastruloids generated from scRNA-seq data. Colors represent cell types. Right, stacked plots showing percentages of the indicated cell types per condition.

G. Schematic illustration of *ex utero* mouse embryo culture conditions.

H. IF staining of E9.0 ex utero cultured embryos for fore-/midbrain marker OTX2 and forebrain/spinal cord marker PAX6. Dash lines show areas of interest. A: Anterior, P: Posterior. Scale bars, 100 µm.

brain, gut endoderm, and mesoderm cells have synchronously progressed to ~E9.0 transcriptionally. We conclude that HAP-gastruloids contain stage-appropriate tissues along the entire A-P axis, which together form a substantially developed embryo model of ESC origin.

Hypoxia boosts the neural patterning of HAP-gastruloids along the A-P axis

The robust representation and patterning of neural cells in HAP-gastruloids is achieved by differentiating the aggregates under hypoxia prior to elongation. We next tested whether hypoxia is essential to gain anterior neural fates. For this, we generated A-P assembloids under normoxia (referred to as NAP-gastruloids, Figure 3A). NAP-gastruloids are built by assembling 2 aggregates instead of 3, since aggregates A and B are effectively the same in the absence of hypoxia. Compared to HAP-gastruloids, fewer NAP-gastruloids contained an OTX2+ region (Figure 3B-C), with the number of OTX2+ cells significantly reduced in the anterior domain (Figure 3D). PAX6 expression was more severely reduced, with less than 10% of NAP-gastruloids harboring OTX2+/PAX6+ (forebrain) cells in comparison to 80% HAP-gastruloids (Figure 3B-D). This is not due to an inherent barrier of the normoxic cells against specifying anterior neural fates, because the 'brain' aggregate (anterior aggregate) when cultured alone expressed and patterned OTX2+/PAX6+ cells (Figure 3E). ScRNA-seq analysis confirmed these findings and showed that NAP-gastruloids formed no forebrain, had a less expanded midbrain and instead showed spinal cord overrepresentation (Figure 3F). Additionally, NAP-gastruloids did not express gut endoderm, as neither scRNA-seq analysis nor FOXA2 staining showed gut derivatives (Figure 3F, S7A). We concluded that hypoxia significantly promotes anterior neural fates and endoderm during cellular self-organization and differentiation, eventually boosting A-P axis neural patterning and gut formation in HAP-gastruloids.

In order to test whether the developing mouse embryo uses its hypoxic microenvironment to mold neural cell fates as observed in the HAP-gastruloid model, we harvested mouse mid-gastrulation embryos and cultured these *ex utero*[31] either in gradual decreasing hypoxia or continuous normoxia starting from E7.5 (Figure 3G). At E9.0-equivalent stage, embryos were collected and stained for PAX6 and OTX2 (Figure 3H, S7B). Both normoxic and hypoxic embryos continued to develop in culture, with hypoxic ones showing nearly 30% higher efficiency and stage-appropriate morphology by E9.0 as reported before[31]. When deeply examining the embryos, we observed that normoxic culture particularly impaired forebrain formation, as normoxic *ex utero* embryos showed severely reduced PAX6 expression compared to hypoxic ones (Figure 2H). Normoxic embryos additionally showed a more restricted OTX2 expression similar to NAP-gastruloids along with spinal cord defects (Figure 3H, S7B). In contrast, hypoxic embryos showed PAX6 and OTX2 expression and neural patterning similar to HAP-gastruloids (Figure 3H, S7B). Together, these results point to hypoxia as a critical microenvironmental effector promoting proper anterior neural development and patterning in both embryo models and embryos.

Hif1a KO HAP-gastruloids show spinal cord and brain defects

The cellular response to hypoxia is mainly mediated by the transcription factor HIF1a[47-49]. To genetically perturb the hypoxia response, we generated *Hif1a* knock-out (KO) ESCs by deleting the first six exons of the gene homozygously (Figure S8A-D). Using these, we then generated *Hif1a* KO HAP-gastruloids and thoroughly characterized them by immunostaining and scRNA-seq (Figure 4A-I, S8E). *Hif1a* KO HAP-gastruloids showed severe neural tube defects, with less than 30% showing a continuous neural tube (Figure 4A-C, S8E). This neural tube defect was not observed in *Hif1a* KO NAP-gastruloids (normoxic culture, Figure S8F), further suggest-

Figure 4 : *Hif1a* KO compromises neural tube and forebrain

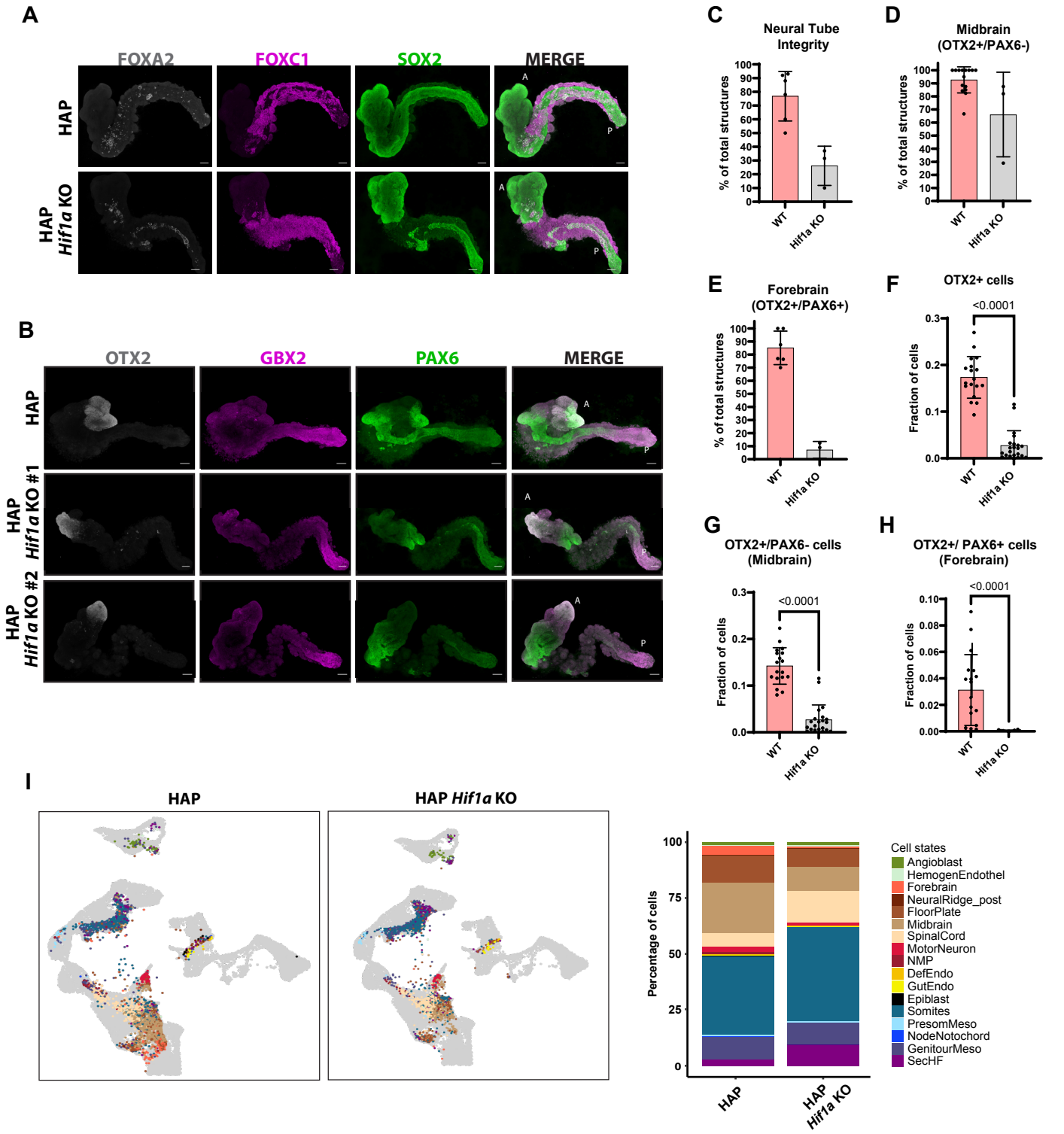

A. IF staining of wt and *Hif1a* KO HAP-gastruloids for neural marker SOX2, somitic marker FOXC1 and endoderm marker FOXA2. A: Anterior, P: Posterior. Scale bars, 100 µm.

B. IF staining of wt and *Hif1a* KO HAP-gastruloids for fore-/midbrain marker OTX2, hindbrain/NMP marker GBX2 and forebrain/spinal cord marker PAX6. A: Anterior, P: Posterior. Scale bars, 100 µm.

C-E. Percentage of total structures per biological replicate showing midbrain and forebrain formation in wt and *Hif1a* KO gastruloids. Column height and error bars indicate mean and standard deviation. Each dot represents a different biological replicate. HAP-gastruloids: For neural tube integrity 6 biological replicates were used (total number 600 individual structures, 461 of which had an integral neural tube along the A-P axis). For midbrain formation 15 biological replicates were used (total number 228 individual structures, 207 of which successfully formed midbrain). For forebrain formation 6 biological replicates were used (total number 67 individual structures, 56 of which successfully formed forebrain). *Hif1a* KO HAP-gastruloids: For neural tube integrity 3 biological replicates were used (total number 66 individual structures, 18 of which had an integral neural tube along the A-P axis). For midbrain formation 3 biological replicates were used (total number 33 individual structures, 20 of which formed midbrain). For forebrain formation 2 biological replicates were used (total number 19 individual structures, 3 of which formed forebrain).

F-H. Fraction of cells per structure expressing OTX2+, OTX2+/PAX6- (midbrain) and OTX2+/PAX6+ (forebrain) cells in wt and *Hif1a* KO gastruloids. Column height and error bars indicate mean and standard deviation. Each dot represents an individual structure, wt: 18 structures from 2 biological replicates, *Hif1a* KO: 21 structures from 2 biological replicates. Statistical test is unpaired two-tailed t test.

I. Left, UMAP plot of wt and *Hif1a* KO HAP-gastruloids generated from scRNA-seq data. Colors represent different cell types. Right, stacked plots showing percentages of the indicated cell types per condition.

ing that the formation of neural tube is neither hypoxia nor HIF1a dependent. Notably, *Hif1a* KO severely compromised anterior neural fates, with less than 10% forming a PAX6+ forebrain domain in comparison to 85% in the wild-type (Figure 4B, D-H). Similar to normoxic ex utero embryos and NAP-gastruloids, *Hif1a* KO HAP-gastruloids showed a restricted capacity to express OTX2+ midbrain cells (Figure 4B, F-G). These results, supported by scRNA-seq experiments (Figure 4I), suggest that hypoxia promotes anterior neural fates at least in part through HIF1a. These results are reminiscent of the neural phenotype of *Hif1a* KO mouse embryos which show neural tube defects and a loss of forebrain cells[32,50]. We note that, in HAP-gastruloids, anterior neural cells - in contrast to posterior neural tube cells - are only robustly represented in hypoxic wild-type conditions.

Perturbation of the TGFβ/BMP pathway hinders neural fate commitment and patterning in HAP-gastruloids

We next set out to investigate whether the hypoxia response in HAP-gastruloids is channeled through any of the primary pathways that are involved in brain specification during mouse embryo development, such as TGFβ and BMP, to shape neural patterning. Precise spatial and temporal regulation of the TGFβ superfamily, i.e. TGFβ, BMP and Nodal signaling, is critical for proper neural induction and subsequent brain development during gastrulation[51]. Specifically, TGFβ, BMPs and Nodal signaling must be antagonized at the anterior end of the epiblast to allow commitment towards anterior neural fates and establish the rostrocaudal boundaries in the developing brain[52-56]. At the same time, however, BMP activation is essential for dorsalization of the neural tube[57-59]. Rationalizing that hypoxia may modulate these pathways, we performed a series of perturbation experiments to increase or decrease their activities in HAP-gastruloids. For this, we treated the HAP-gastruloid 'brain' aggregate (aggregate C) with one of the following for 24h between 48-72h: TFGβ protein (2 ng/ml), TGFβ/Nodal inhibitor SB-431542 (10 uM), BMP inhibitor Noggin (100 ng/ml) (Figure 5A), BMP4 (10 ng/ml) or BMP7 (25 ng/ml) (Figure S9A). The applied concentrations are used in liver and brain organoid generation[44,60-63].

Fluorescence staining and A-P quantifications showed that TGFβ supplementation significantly reduced midbrain and forebrain formation (fewer OTX2+/PAX6+ cells, Figure 5B-D, S10), whereas TGFβ inhibition overcommitted cells towards forebrain and compromised compartmentalization (more OTX2+/PAX6+ cells, Figure 5B-C, S10). BMP4 supplementation completely altered HAP-gastruloid morphology and remained inconclusive (Figure S9B). Notably, BMP inhibition and BMP7 supplementation severely reduced forebrain but not midbrain commitment (Figure 5B-D, S9C-F), indicating that TGFβ and BMP pathways distinctly regulate mid- and forebrain regionalization. These results suggest that hypoxia may enable the commitment to diverse anterior neural fates at least in part by modulating TGFβ and BMP expression levels.

Anterior forebrain development in HAP-gastruloids with WNT inhibition

Despite robust commitment and compartmentalization of anterior neural cells in HAP-gastruloids, the absence of the most rostral forebrain markers remained a major limitation to studying the full complexity of the brain (Figure 2H, 6A). During organogenesis, around E11, the anterior forebrain forms the telencephalon, which gives rise to the cortex, the center of mammalian cognition. Although telencephalon expands around E10, the telencephalic primordium is specified at 8.5, marked by the expression of the forkhead transcription factor gene FOXG1 [64,65] (Figure 6B). Given that during gastrulation the most anterior end of the epiblast (future rostral forebrain) is exposed to signals that inhibit WNTs emanating from the extraembryonic tissues [66-68], we rationalized that residual WNT activity or insufficient WNT inhibition in HAP-gastruloids could hinder anterior forebrain

Figure 5 : Brain formation in HAP-gastruloids is hindered by perturbations of TGFβ/BMP

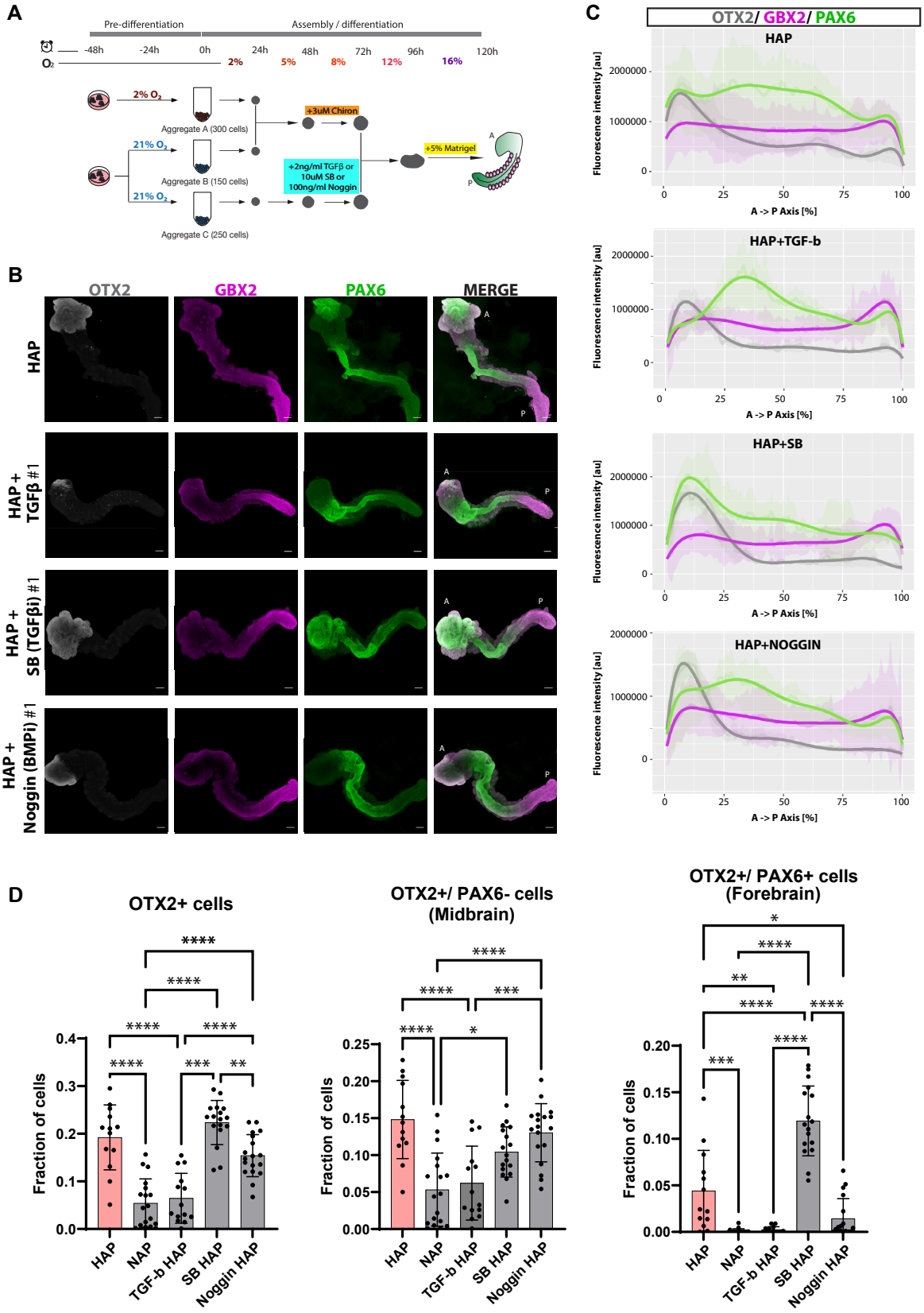

A. Schematic illustration of the experimental pipeline for treating HAP-gastruloids with TGFβ, SB or Noggin.

B. Left, IF staining of HAP, HAP+TGFβ, HAP+SB and HAP+Noggin for fore-/midbrain marker OTX2, hindbrain/NMP marker GBX2 and forebrain/spinal cord marker PAX6. A: Anterior, P: Posterior. Scale bars, 100 µm. Right, Localization of OTX2, GBX2 and PAX6 signals along the A-P axis of each condition. Lines show mean values from 10 individual structures.

C. Localization of OTX2, FOXG1 and PAX6 signals along the A-P axis of HAP, HAP+TGFβ, HAP+SB and HAP-+Noggin. Lines show mean values from 10 individual structures

D. Fraction of cells per structure expressing OTX2+, OTX2+/PAX6- (midbrain) and OTX2+/PAX6+ (forebrain) cells in HAP, HAP+TGFβ, HAP+SB and HAP+Noggin. Column height and error bars indicate mean and standard deviation. Each dot represents an individual structure. HAP-gastruloids: a total of 13 individual structures from 1 biological replicate were used. HAP+TGFβ: a total of 14 individual structures from 2 biological replicates were used (7 structures/ biological replicate). HAP+SB: a total of 17 individual structures from 2 biological replicates were used (8-9 structures/biological replicate). HAP+Noggin: a total of 18 individual structures from 2 biological replicates were used (9 structures/biological replicate). Statistical test is one-way ANOVA with multiple testing correction. P-values **** p<0.001, ** p<0.005, *p<0.05

formation. We thus tested whether exogenous WNT inhibition (WNTi) could further promote brain anteriorization by treating the 'brain' aggregate (aggregate C) with the WNT inhibitor XAV-939 (Figure 6C, HAP+XAV' condition, treatment window is 48-72h). Remarkably, WNTi under hypoxia induced robust, but not ectopic, FOXG1 expression and the majority of HAP+X structures expressed FOXG1 in a similar pattern to the E8.75 embryo (Figure 6C-H, S11A). The total fraction of OTX2+ cells remained similar between HAP and HAP+XAV, however the spatial organization of the brain compartments was more advanced in HAP+XAV, with midbrain, posterior forebrain, and anterior forebrain regions clearly distinguishable from each other (Figure 6D-I). ScRNA-seq validated these results, as anterior forebrain markers Lhx2, Six3 and Foxg1 were expressed in HAP+XAV (Figure 6J, S11B-D). Surprisingly, spinal cord ventral markers such as Nkx6.1 and Olig2 were also expressed at the cost of dorsal marker Zic1 and Pax3, but not Pax6 (S11D) while somites and presomitic mesoderm representation was overall reduced (Figure 6J). However, WNTi impaired the elongation of HAP-gastruloids, probably due to its residual effect on the posterior aggregates (Figure S11E-F). In conclusion, WNT inhibition of the 'brain' aggregate (aggregate C) expanded anterior and posterior neural representation in HAP-gastruloids.

Finally, in order to test whether TGFβ or Wnt inhibition can substitute hypoxia for the formation of a well-developed and patterned brain domain in HAP-gastruloids, we treated NAP-gastruloids (normoxic assembloids, Figure 2A) with either SB or XAV or both (Figure S12A). In line with this, TGFβ inhibition of NAP-gastruloids yielded an expanded OTX2+ midbrain domain, but not OTX2+/PAX6+ forebrain (S12B), while WNT inhibition of NAP-gastruloids yielded an OTX2+ midbrain domain, occasionally (40%) OTX2+/PAX6+ posterior forebrain, but no FOXG1+/OTX2+ anterior forebrain (Figure S12C). Inhibition of both TGFβ and Wnt pathways advanced the anterior neural patterning as almost all structures formed OTX2+ midbrain and OTX2+/PAX6+ posterior forebrain domains, but no FOXG1+/OTX2+ anterior forebrain (Figure S12D). Based on these results, we concluded that external cues do not substitute hypoxia treatment and that hypoxia-driven cell-intrinsic regulation of TGFβ in combination with exogenous Wnt inhibition are necessary for advanced anterior neural patterning in HAP-gastruloids.

DISCUSSION

The developing embryo does not emerge from the simple assembly of distinct parts. It is only through the study of stem cell-derived aggregates that the concept of modularity begins to emerge. While the formation of the HAP-gastruloid does not serve as a direct replica of the embryonic process, it provides valuable insights into the principles of cellular interactions within multicellular systems. Importantly, we emphasize that HAP-gastruloids were not developed to perfectly mimic the embryo. Instead, our investigation of hypoxia as a critical microenvironmental factor led to the development of HAP-gastruloids, which in turn facilitated the study of interactions between different cellular populations within these aggregates.

Similar to other in vitro systems, such as ESC cultures and gastruloids, HAP-gastruloid selectively recapitulates key aspects of embryogenesis. The primary contribution of HAP-gastruloids lies in their ability to open new avenues for investigating cellular processes that are otherwise inaccessible in embryos. In our model, we chose to use ESCs without the support of extraembryonic cells, simplifying the system and enabling us to focus specifically on decision-making within the epiblast. The assembly approach, when combined with hypoxia, recreates the natural morphogen gradients in the epiblast, ultimately yielding a unified embryo model with anterior-posterior (A-P) patterning characteristic of early development.

Often referred to as a detrimental element in somatic tissues, hypoxia is an integral part of

Figure 6 : Wnt inhibition induces anterior forebrain

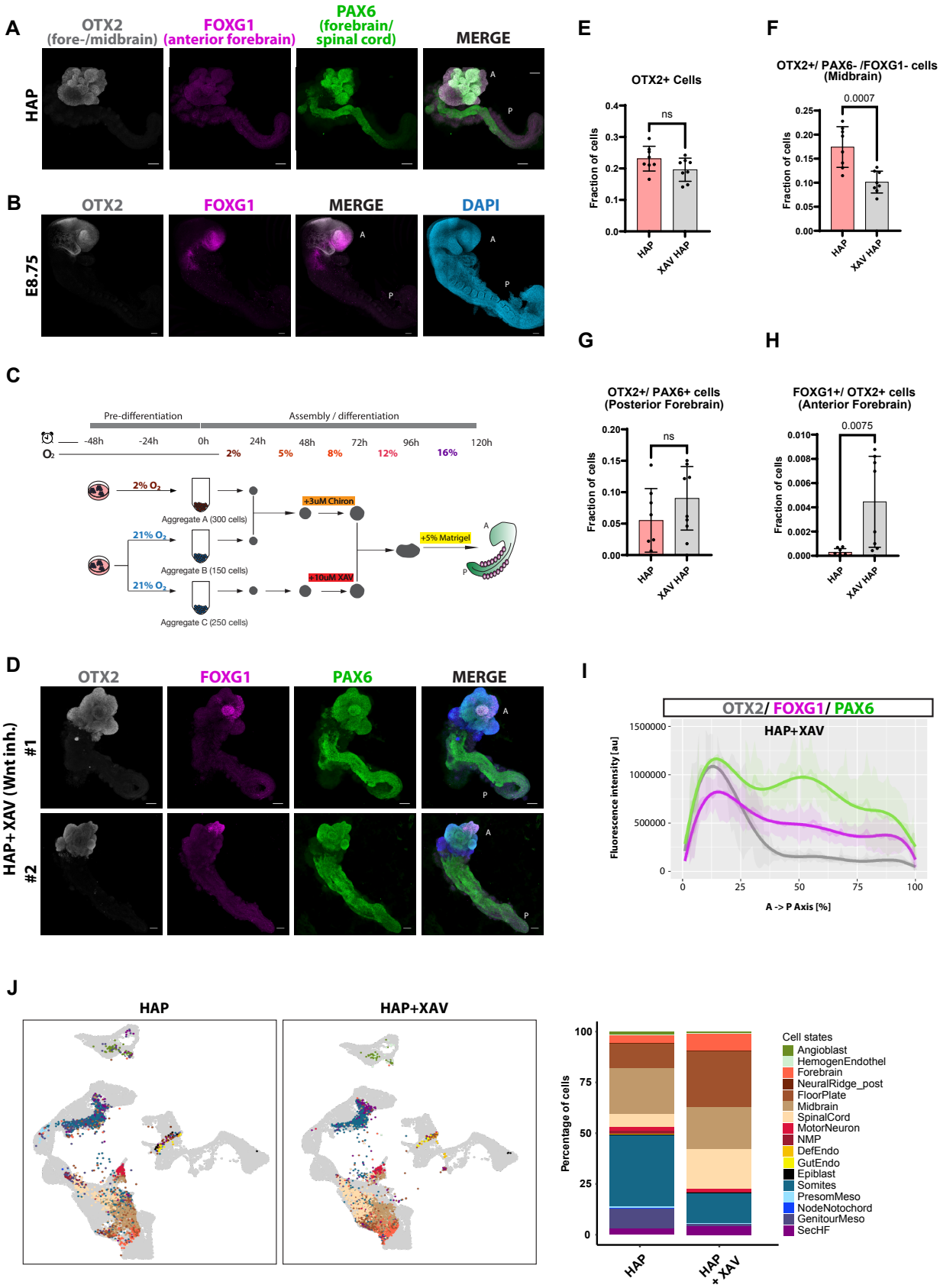

A. IF staining of HAP-gastruloids for fore-/midbrain marker OTX2, anterior forebrain marker FOXG1 and forebrain/spinal cord marker PAX6. A: Anterior, P: Posterior. Scale bars, 100 µm

B. IF staining of E8.75 mouse embryo for fore-/midbrain marker OTX2, anterior forebrain marker FOXG1 and forebrain/spinal cord marker PAX6. A: Anterior, P: Posterior. Scale bars, 100 µm

C. Schematic illustration of the experimental pipeline for treating HAP-gastruloids with XAV.

D. IF staining of HAP+XAV for fore-/midbrain marker OTX2, anterior forebrain marker FOXG1 and forebrain/spinal cord marker PAX6. A: Anterior, P: Posterior. Scale bars, 100 µm

E-H. Fraction of cells per structure expressing OTX2+, OTX2+/PAX6- (midbrain) and OTX2+/PAX6+ (posterior forebrain) and OTX2+/FOXG1+ cells in HAP- and HAP+XAV**.** Column height and error bars indicate mean and standard deviation. Each dot represents an individual structure. HAP: a total of 8 individual structures from 1 biological replicate were used. HAP+XAV: a total of 8 individual structures from 1 biological replicate were used. Statistical test is unpaired two-tailed t test.

I. Localization of OTX2, FOXG1 and PAX6 signals along the A-P axis of HAP+XAV. Lines show mean values from 10 individual structures.

J. Left, UMAP plot of HAP and HAP+XAV generated from scRNA-seq data. Colors represent different cell types. Right, stacked plots showing percentages of the indicated cell types per condition.

mammalian development. In addition to inducing a metabolic shift away from oxidative phosphorylation and towards glycolysis, hypoxia can affect the transcriptional profile through HIF1a and/or by altering the activity of histone and DNA demethylases[30,69]. The hypoxia-driven cell type diversification and compartmentalization in our system is largely mediated by HIF1a, as Hif1a KO HAP-gastruloids show compromised neural commitment. Our findings in the HAP-gastruloid model are consistent with the embryonic phenotypes of Hif1a and Hif2a KO mice that show neural tube and brain defects, including perturbation of forebrain patterning[32,50]. Additionally, the HAP-gastruloid model now allows spatial dissection of such phenotypes, by e.g. creating anterior-only KOs.

We show that the benefit of hypoxia is negated upon perturbation of TGFβ levels, suggesting that TGFβ expression is oxygen-sensitive in our system similar to others[70,71]. It is plausible that TGFβ is directly regulated by HIF1a or through mechanisms independent of HIF1a or through other effectors downstream of HIF1a, eventually resulting in TGFβ inhibition. Additionally, considering BMP signaling is necessary for dorsal patterning, it is plausible that hypoxia regulates selective BMPs for dorsal patterning of the forebrain, as BMP inhibition disrupts dorsal forebrain (PAX6 expression) but no midbrain formation. However, whether BMPs are regulated by hypoxia and if this regulation is driven by HIF1a remains to be seen in further studies. In summary, our findings build on and uniquely expand decades of key research on the effects of hypoxia by revealing its key influence in the developing embryo and our embryo model.

Beyond investigating hypoxia, HAP-gastruloids offer a unique model to investigate self-organizing properties and patterning events beyond the findings presented here. We show that the assembled aggregates that make up the HAP-gastruloids form a homochronic entity at 120h. We also show that the 'brain' aggregate distinctly forms the anterior neural 'brain-like' region of HAP-gastruloids, while the other Chiron-treated aggregates form the posterior tissues. Notably, it is the integration of these anterior and posterior regions and the interaction between them that forms a continuous neural tube and presumably other more anterior tissues such as anterior somites and endoderm. Beyond the specification and patterning of brain cells, it remains to be seen which of these anterior tissues result from hypoxia and/or A-P assembly. Overall, HAP-gastruloid is a unique embryo model that can be used to address key open questions otherwise concealed by the uterine microenvironment.

ACKNOWLEDGMENTS

We thank members of the Bulut-Karslıoğlu Lab and Alfonso Martinez Arias, Jesse Veenvliet, Matthew Kraushar, Sigmar Stricker, Ludovic Vallier, and Teresa Rayon for discussions; MPIMG facilities, especially microscopy, for excellent service and discussions. We thank Can Aztekin, Kelly Hu, and Marion Leleu for help with scRNA-seq. We thank Maria Walther, Susanne Lade, Astrid Grimme, Cordula Mancini, Birgit Romberg, Shelby Baumgartner, Edda Einfeldt for assistance. Work in the Hanna Lab is supported by MBZUAI-WIS Program grant, a Minerva Stiftung grant, and ERC-COG-2022 #101089297–ExUteroEmbryogenesis. Work in the Kretzmer Lab is supported by the Hasso Plattner Institute and the Max Planck Society. Work in the Bulut-Karslioğlu Lab is supported by the Max Planck Society, and Humboldt Foundation (Sofja Kovalevskaja Award), the European Research Council (ERC) under the European Union's Horizon 2020 research and innovation programme (ERC grant agreement no. 101117421, 'DOR CODE'').

AUTHOR CONTRIBUTIONS

Conceptualization: AB and AB-K. Methodology: AB and AB-K. Investigation: AB, HÖÖ, IB. Formal analysis: IK, PAO, RB. Visualization: AB, IK, RB. Writing - original draft: AB and AB-K. Supervision: JHH, HK, AB-K. Funding acquisition: JHH, HK, AB-K.

DECLARATION OF INTERESTS

JHH has filed for patents involving ex utero embryogenesis. The other authors declare no conflict of interest.

METHODS

Animal experimentation

All animal experiments were performed according to local animal welfare laws and approved by local authorities (Landesamt für Gesundheit und Soziales). Mice were housed in individually ventilated cages and fed ad libitum.

Mouse ESC culture

F1G4 and FK223 (originally from Bernhard Herrmann) and KH2 (originally from Konrad Hochedlinger) mouse cell lines were used. mESCs were routinely maintained on 6cm plates (Corning, 430166) gelatinized with 0.1% gelatin (1:20 dilution of 2% gelatin (Sigma, G1393) in tissue-culture grade H_2O) and coated with mitotically inactive primary mouse embryo fibroblasts (3-4x10^4cells/cm²). They were cultured in Knockout Dulbecco's Modified Eagle's Medium (KO-DMEM) (Thermo Fisher Scientific 10829-018) supplemented with 15% FBS (Thermo Mexico origin serum, Thermo cat# 10438026, lot# 2535232RP), 1% GlutaMAX (GIBCO, 35050038), 1% nucleosides (EmbryoMax Nucleosides (100x, Merck, ES-008-D), 0.2% beta-mercaptoethanol (Thermo Fisher Scientific, 21985023), Penicillin-Streptomycin (10,000 U/mL) (GIBCO, 15140122), and 1000 U/mL homemade LIF and grown at 37°C in a 20% O_2 and 5% CO_2 incubator unless otherwise specified. Hypoxic ESCs were grown in 2% O_2. mESCs were split every second day with a dilution suitable to the proliferation velocity (between 1:5 and 1:9). mESC+LIF medium was refreshed daily. For splitting, media was aspirated and cells were washed once with PBS and dissociated with TrypLE (Thermo Fisher Scientific 12604-021) for 5-10 min at 37°C. TrypLE was neutralized by 3 ml mESC+LIF and cells centrifuged for 5 min at 1000 rpm, after which the pellet was resuspended in mESC+LIF. For freezing of mESCs, cell pellets were resuspended in mESC medium with 20% FCS, and mixed in a 1:1 ratio with mESC freezing medium. Cells were frozen down o/n in the –80 °C and transferred to liquid nitrogen the next day. All figures show stainings from F1G4 cell lines unless stated otherwise.

HAP-/ NAP-gastruloid generation

mESCs were cultured in either hypoxia and normoxia. At the onset of HAP-gastruloid generation, normoxic and hypoxic mESCs were trypsinized, washed with mESC medium and resuspended as single cells. After MEF depletion, mESCs were pelleted and resuspended in PBS. After another wash, cells were resuspended in pre-warmed NDiff227 (Takara, XA0530) and counted with Countess 3 (Invitrogen, 16842556). Cells were plated in a 96-U-bottom, ultra-low attachment plate (Costar, 7007) to from three distinct aggregates: aggregate A (300 cells), aggregate B (150 cells) and aggregate C (250 cells).

Aggregates A and B were fused at 24h and treated with 3 uM Chiron at 48h. Aggregate C was grown separately without being treated with Chiron and at 72h fused with the other aggregates. At 96 h, 5% matrigel (corning/BD, 356231) was added. At 120 h, structures were collected for further processing. Structures were grown in a hypoxic incubator at 37°C and 5% CO_2 in a gradually increasing oxygen setup. NAP-gastruloids were generated following the same procedure but cultured in 21% O_2.

Generation of *Hif1a* KO mouse ESCs

Hif1a KO gene was knocked out with CRISPR/Cas9 gene editing tool. More specifically the first six exons of the gene were removed by gRNAs targeting upstream of exon 1 (TCAGAGAACTCTATAGAGAGCCG) and

downstream of exon 6 (TTGTACGTCCACTGTATCCAAAG). gRNA sequences were cloned into the pX330A-1x2 plasmid. Wild-type F1G4 cells were nucleofected with the plasmids using the Lonza 4D Nucleofector. After 48 h, cells were single-cell sorted into 96-well plates using the BD FACSAria Fusion (Software v8.0.1). 8-10 days later clones were selected and expanded. After expansion DNA was extracted for each clone and screened using two primer pairs:

Primer pair 1: Knockout Primers, amplicon size 767 bp, amplified only if KO is successful.
F: 5′-GAGAGGTTTGGCAAGACGGAT-3′
R: 5′-TGTGCAAGGGATGTTGCCTAA-3′
Primer Pair 2: Control Primers, amplicon size 653 bp, amplified only if KO is unsuccessful.
F: 5′-AGTGGCTAAGGAAGTAAGCACC-3′
R: 5′-ACATTGTGGGGAAGTGGCAA-3′

DNA extraction

Cells were grown until confluent enough. Lysis buffer was added and cells were incubated overnight at 37°C. Next day ice cold NaCl/EtOH was added for 2h/RT, until proper precipitating DNA was visible. DNA was then washed 3x with 70% EtOH and air dried for 15-20 minutes. Finally DNA was resuspended with the desired volume of H2O by overnight incubation at 37°C. For subsequent genotyping PCR usually 1 or 2 ul DNA was used as a template.

RNA extraction and RT-qPCR

Total RNA was extracted using the QIAGEN RNeasy kit (QIAGEN, 74004), following the manufacturer's instructions and 5 µg of RNA was used as input to generate complementary DNA (cDNA) with the High-Capacity cDNA Reverse Transcription Kit (Thermo Fisher Scientific, 4368814). cDNA was used to perform real-time quantitative PCR (qPCR) using primers designed to amplify different exons of *Hif1a* using KAPA SYBR FAST qPCR Master Mix (2X) ABI Prism (Thermo Fisher Scientific, KK4617) on the QuantStudio 7 Flex Real-Time PCR System (Applied Biosystems) thermal cycler. In RT-qPCR experiments, data represent $\log_2$FC over *mTbp*.

Primers used:
Exon2_3:
F: 5′-TCTCGGCGAAGCAAAGAGTC-3′
R: 5′-AGCCATCTAGGGCTTTCAGATAA-3′
Exon5_6:
F: 5′-GATGACGGCGACATGGTTTAC-3′
R: 5′-CTCACTGGGCCATTTCTGTGT-3′
Exon10_11:
F: 5′-ACCTTCATCGGAAACTCCAAAG-3′
R: 5′-CTGTTAGGCTGGGAAAAGTTAGG-3′
mTbp:
F: 5′-CCTTGTACCCTTCACCAATGAC-3′
R: 5′-ACAGCCAAGATTCACGGTAGA-3;

Nucleofection of ESCs

Nucleofection was performed according to Amaxa UD-Nucleofector Protocol provided by the company. Amaxa 4D Nucleofector kit (Lonza V4XP-3024) and 4d-Nucleofector unit were used.

Ex utero embryo culture

Ex utero culture was performed as described in[31]. All embryos were dissected at E7.5, immediately moved to roller culture, grown in EUCM medium and harvested one and a half days later (E9.0). During roller culture two different O_2 conditions were tested as indicated.

Inhibitor/Growth Factor treatments

Growth factors and inhibitors used as stated in accordingly throughout the study: for exogenous WNT activation: 3 uM Chiron (CHIR99021, Sigma, SML1046), for exogenous TGFβ supplementation: 2 ng/ml TGFβ (Biotechne, 240-B-010), for TGFβ and Nodal inhibition: 10 uM SB 431542 (Tocris, 1614/10), for BMP signalling inhibition 100 ng/ml Noggin (Recombinant Human Noggin/Fc Chimera, CF 50 ug, R&D Systems, 3344-NG-050), for exogenous BMP4 supplementation 10 ng/ml BMP4 (R&D Systems, 314-BP-500/CF), for exogenous BMP7 supplementation 25 ng/ml BMP7 (Thermo Fisher, PHC9544), for WNT inhibition: 10 uM XAV939 (MedChemExpress, HY-15147) and 1uM LGK974 (BIOTREND, 331-21058-1).

Immunostaining

Whole mount immunofluorescence was performed as described in [9]. Individual HAP-

gastruloids were picked using a p200 pipette with the tip cut-off at the 50 µl mark and transferred to Ibidi 8-well glass-bottom plates (Ibidi, 80827). HAP-gastruloids were washed twice with PBS + $MgCl_2$ and $CaCl_2$ + 0.5% BSA (Sigma, D8662), once with PBS, and then fixed in 4% PFA for 1h at 4°C on a rocking platform. Subsequently, HAP-gastruloids were washed twice in PBS for 5 min, permeabilized by 3 x 20 min incubation in 0.5% Triton-X/PBS (PBST) and blocked in 5% fetal calf serum/PBST (blocking solution) overnight at 4°C. Primary antibody incubation was performed in blocking solution for 48-72h at 4°C, after which HAP-gastruloids were washed three times with blocking solution and three times with PBST. After the last washing step, HAP-gastruloids were incubated in blocking solution overnight at 4°C. The next day, secondary antibodies diluted in blocking solution were added, and structures were incubated for 24h at 4°C. Afterwards, HAP-gastruloids were washed three times with blocking solution and three times with PBST, followed by DAPI (0.02%, Roche Diagnostics, 10236276001) in PBS overnight incubation. Next day DAPI was removed and HAP-gastruloids were washed once with PBS and then processed further for tissue clearing (see below). Primary antibodies used in this study include: OTX2 (Polyclonal Goat IgG, R&D Systems, AF1979), PAX6 (mouse hybridoma, DSHB (concentrated)), PAX6 (Polyclonal Rabbit IgG, BioLegend, 901301), GBX2 (Polyclonal Rabbit IgG, Proteintech, 21639-1-AP), FOXG1 (Monoclonal Rabbit IgG, Abcam, [EPR18987] ab196868), FOXC1 (Monoclonal Rabbit IgG, Abcam, [EPR20685] ab227977), FOXA2 (Polyclonal Goat IgG, R&D Systems, AF2400), SOX2 (Monoclonal mouse IgG2a, Santa Cruz, sc-365964). All primary antibodies were used in a dilution 1:200, apart from GBX2 (1:100) AND PAX6 (mouse hybridoma, 1:50). Secondary antibodies used in this study include: Donkey anti-Goat IgG (H+L) Cross-Adsorbed Secondary Antibody, Alexa Fluor™ 647 (Thermo, A21447), Donkey anti-Mouse IgG (H+L) Highly Cross-Adsorbed Secondary Antibody, Alexa Fluor Plus 488 (Thermo, A32766) and Donkey anti-Rabbit IgG (H+L) Highly Cross-Adsorbed Secondary Antibody, Alexa Fluor 546 (Thermo, A10040). All secondary antibodies were used in a dilution 1:250.

Tissue clearing

Prior to imaging, HAP-gastruloids were cleared with RIMS (Refractive Index Matching Solution). To this end, samples were washed twice with PBS for 10 min, post-fixed in 4% PFA for 20 min and washed three times with 0.1M phosphate buffer (PB, 0.025 M NaH_2PO_4 and 0.075 M Na_2HPO_4, pH 7.4). Clearing was performed by incubation in RIMS (133% w/v Histodenz (Sigma, D2158 in 0.02M PB) on a rocking platform at 4°C for at least one day. Occasionally, HAP-gastruloids were embedded in agarose before cleared with RIMS. To this end, 1.5% low melting point (LMP), analytical grade (Promega, V2111) agarose was prepared in PBS, incubated at 80°C for 15 min, and cooled down to 37°C for 3 min in a thermomixer. The pipette was set to 20 µl and HAP-gastruloids were stabilized on the ibidi plate with a drop of LMP agarose for 5 min until the agarose was dry.

Image acquisition

Confocal images were acquired on a Zeiss LSM 880 confocal running under ZEN Black 2.3 (Zeiss Germany). All structures were captured in z-Stacks with an Airydetector in FastAiryMode. The individual structures were recorded in tile scans using a Plan-Apochromat 20x and a numerical aperture of 0.8. The lateral (xy) resolution was 0.25 µm per pixel, furthermore a distance of 10 µm was chosen for the axial (z) resolution in order to image an average nucleus diameter and to avoid oversampling of signals for later expression analyses. The airy data were processed and prelayd for several downstream analysis.

Wide field images were acquired using the Zeiss Celldiscoverer 7 running under Zen Blue 3.7 (Zeiss Germany). Also here structures were captured in z-stack with an Axiocam 712. An 5x PlanApochromat with a numerical aperture of 0.35 and a 3x3 camera binning achieved a lateral resolution of 2.09 µm per pixel, also here the slice height was captured with 10 µm. Each captured structure was located in a single mold of 96-well

ultra-low attachment plate and served as a single field of view.

Image Processing

Maximum Intensity Projections were used to quantify the expression of key markers along the morphological axes. To generate these in batches from raw 3-dimensional confocal data, we used a self-made script in ZEN 3.8 blue in the module "Open Application Development" as well as functions of the module "Advanced Processing". Batched airyscan processing of confocal data was performed on a dedicated workstation running under ZEN Black v2.3 (Zeiss, Germany).

Image Analysis

Single cell measurements in full embryos were performed using Zen Blue and the additional module "Image Analysis" running under v3.5 (Zeiss, Germany). All confocal data was processed with the identical fully automated pipeline using a classical segmentation algorithm. Herein, the nuclear counterstain was smoothed, the background was subtracted and thus the foreground was one-sided normalized, a local relative threshold followed by a fixed threshold, 2 iterations of binary command open followed by classical water shedding. The masks obtained were filtered to achieve a size between 100-1000 μm^2. The resulting masks were projected back onto the original image to quantify intensities and geometries. This procedure was batched within ZEN and resulted in about $5\text{-}10 \times 10^5$ single cells per quantified structure.

Morphometrical analysis and profiling analysis were performed in a custom ImageJ/Fiji macro. In summary, initial objects were determined on counterstainings (nuclei or transmittance images) using variance-based thresholds. To create these masks, the images were set to 0.01 times their original area, variance filtered, threshold and brought back to their original size. The resulting binary image was used for object identification. Once the structure was identified as ROI it was back on the raw data and morphometrics were measured. The primary object was further used in the pipeline to determine an anterior-posterior line using a custom-built algorithm. For this, the primary mask was projected onto a monochromatic background, the resulting surface was skeletonized and geodesic diameters were used to find the longest connected segment, which is typically the AP axis. This secondary object was fitted to a total of 50 intervals the resulting length of the axis was included in the morphometrics. Furthermore, the axis was used to straighten the complex embryo structures in order to extract a marker expression and a width profile from the structures. All profiles were adjusted to a length of roughly 1000 pixel to enable a direct comparison over multiple conditions.

Statistics

Cell counting analysis of the individual data was undertaken with the help of customer R-Script. The raw data from the result of the measurements were used. We identified 74942 +/- 22270 (mean+sd) per structure. The proportions of the different marker-positive cells were determined by algorithmic and in a further step controlled by the experimenter. For visualization, density plots between all channels were used to get a quantitative idea of the decompositions, furthermore, result tables from these results were used for a simplified visualization for the reader. Only mean intensities were used for this approach as they are robust to any segmentation irregularities.

Further, the script binned the profile to achieve a length of 100 units per profile independent of the initial axis lengths, enabling the reader to evaluate the relative marker abundance along the AP-axis. For easier visualization we fitted a 6th order polynom (saturated) over the averaged results (opaque) and standard deviation (more Oaque), on top of the raw data.

Single-cell RNA-seq

HAP-gastruloids, NAP-gastruloids, *Hif1a* KO and +XAV samples: Single-cell RNA-sequencing (scRNA-seq) experiments were performed with Parse Biosciences (Evercode, Cell Fixation v3) and samples were fixated according to user manual (Evercode Cell Fixation kits Reagents

CF100) and enhancer (CF200)). Briefly, approximately 20 structures per condition were collected in a 1.5 ml protein low binding tube filled with cold PBS. After two subsequent washes with cold PBS, 300 ul TrypLE was added in each tube and the suspension was incubated for 20 minutes at 37°C, with pipetting up and down every 10 minutes till all cells were dissociated. The cell suspension was resuspended in 600 ul PBS, spinned down (4°C, 500g, 5min) and the pellet was resuspended in 1 ml PBS. After counting the desired number of cells (between 10^5-10^6cells) each sample was transferred in a new Protein Low Binding 1.5 ml tube and centrifuged at 4°C, 500xg, 5 min. Pellet was resuspended in 187.5 ul Prefixation Master Mix (see user manual for every Master Mix preparation), strained into a new 1.5 ml tube and mixed with 62.5 µL of Cell Fixative Master Mix. After a 10-minute incubation on ice, 20 µl of Permeabilization Solution were added and the sample was incubated on ice for 3 minutes. After incubation sample was mixed with 250 ul Fix and Perm Stop Buffer and spinned down (4°C, 500xg, 5 min). The pellet was resuspended in 70 ul Cell Storage Master Mix and strained into a new 1.5 ml tube. Fixed cells were counted and stored at -80°C. Library preparation was performed according to instructions (Parse Biosciences, Evercode Whole Transcriptome Version 3 kit, WT100/WT200). Sequencing was performed on Novaseq.
TLS dataset was a reference dataset generated in our lab following manufacturer's recommendations for Chromium single cell kit (10x Genomics) prior to HAP-/NAP-gastruloid samples.

Data analysis:

Bioinformatics tools

Statistical analyses, computations and plots were executed using R version 4.4.1' "Race for Your Life", unless noted otherwise[72]. For single-cell analysis, the Seurat package version 5.1.0 was utilized[73]. Data distributions were visualized through boxplots using the ggplot2 package[74]. In these boxplots, the central line represents the median, the box defines the interquartile range (IQR) from the 25th to 75th percentile and the whiskers extend to 1.5 times the IQR. Points outside this range are identified as outliers.

Pre-processing

HAP-, NAP-gastruloids, *Hif1a* KO, and +XAV scRNA-seq data were pre-processed by Parse Biosciences. Reads were aligned using STARsolo against a combined reference genome of human (GRCh38) and mouse (mm10), using the parameters --soloFeatures GeneFull_Ex50pAS --soloType CB_UMI_Complex --soloAdapterSequence ATGAGGGGTCAG. UMI and barcode quantification followed alignment. For each sample, 15 objects (3 runs × 5 lanes) were merged into a single Seurat object. These four sample-level objects were subsequently merged into one combined Seurat object for downstream analysis. Cells with fewer than 300 or more than 7000 detected genes and with fewer than 700 or more than 30,000 total counts, were excluded. After filtering, the data was log-normalized, variable features were identified, and data were scaled using Seurat with default parameters.

Cell state annotation and projection

As a foundation for annotation, we used a scRNA-seq reference dataset of WT mouse embryos spanning E6.5 to E9.0, closely following the generation and processing described by Grosswendt et al. (2020) [45]. This WT reference comprises 55 distinct cell state clusters.

For the analysis of neural cell states, the spinal cord cluster from the WT reference was extracted and re-clustered using Seurat. After normalization and scaling, subclustering was performed using FindNeighbors(dims=1:25) and FindClusters(resolution=0.1). The resulting two spinal cord clusters were annotated based on their marker gene expression. In general, cell state-specifc marker genes were identified using FindAllMarkers(only.pos = TRUE, min.pct = 0.05, logfc.threshold = 0.25). Annotation of HAP-, NAP-gastruloid, *Hif1a* KO, +XAV and TLS samples was performed using label transfer via transfer anchors identified with FindTransferAnchors

(reference.reduction = "pca"). WT cell state labels were transferred using TransferData(dims = 1:30).

For visualization, a reference UMAP was computed on a subset of the WT reference, including only cell states present in the HAP-gastruloid sample as determined by label transfer. The UMAP was generated using normalized, scaled and PCA-transformed data (RunUMAP(dims=1:30, return.model=TRUE)). Each sample was then projected onto this reference UMAP using MapQuery(reference.reduction = "pca", reduction.model = "umap"), following anchor identification as described above. For UMAPs of the neural lineages, the WT reference subset was restricted to E8.5-9.0 cells from neural cell states found in the samples (as most cells were predicted to correspond to E9.0 in the developmental stage analysis). The same normalization, dimensionality reduction, and mapping steps were applied as described above. To determine cell state proportions, the number of cells assigned to each state was divided by the total number of cells in the corresponding sample.

To compare marker gene expression across samples, we calculated, for each gene, sample, and label-transferred cell state, the average expression and the percentage of expressing cells by dividing the number of cells with detectable expression by the total number of cells in that sample and cell state.

Developmental stage prediction

To determine the embryonic stage of HAP-, NAP-gastruloids, *Hif1a* KO, +XAV, and TLS cells, we used a normalized subset of the WT reference containing only the cell states present in the respective samples. Label transfer was performed using FindTransferAnchors and TransferData. In addition to assigning each cell to the stage with the highest prediction score, we computed a continuous pseudostage by calculating the prediction score-weighted sum of all stages.

Reference list

1. Tam, P.P., and Behringer, R.R. (1997). Mouse gastrulation: the formation of a mammalian body plan. Mech Dev *68*, 3-25. 10.1016/s0925-4773(97)00123-8.
2. Simon, M.C., and Keith, B. (2008). The role of oxygen availability in embryonic development and stem cell function. Nat Rev Mol Cell Biol *9*, 285-296. 10.1038/nrm2354.
3. Dunwoodie, S.L. (2009). The role of hypoxia in development of the Mammalian embryo. Dev Cell *17*, 755-773. 10.1016/j.devcel.2009.11.008.
4. Houghton, F.D. (2021). HYPOXIA AND REPRODUCTIVE HEALTH: Hypoxic regulation of preimplantation embryos: lessons from human embryonic stem cells. Reproduction *161*, F41-F51. 10.1530/REP-20-0322.
5. Dupont, C. (2024). A comprehensive review: synergizing stem cell and embryonic development knowledge in mouse and human integrated stem cell-based embryo models. Front Cell Dev Biol *12*, 1386739. 10.3389/fcell.2024.1386739.
6. van den Brink, S.C., Baillie-Johnson, P., Balayo, T., Hadjantonakis, A.K., Nowotschin, S., Turner, D.A., and Martinez Arias, A. (2014). Symmetry breaking, germ layer specification and axial organisation in aggregates of mouse embryonic stem cells. Development *141*, 4231-4242. 10.1242/dev.113001.
7. Turner, D.A., Girgin, M., Alonso-Crisostomo, L., Trivedi, V., Baillie-Johnson, P., Glodowski, C.R., Hayward, P.C., Collignon, J., Gustavsen, C., Serup, P., et al. (2017). Anteroposterior polarity and elongation in the absence of extra-embryonic tissues and of spatially localised signalling in gastruloids: mammalian embryonic organoids. Development *144*, 3894-3906. 10.1242/dev.150391.

8. Beccari, L., Moris, N., Girgin, M., Turner, D.A., Baillie-Johnson, P., Cossy, A.C., Lutolf, M.P., Duboule, D., and Arias, A.M. (2018). Multi-axial self-organization properties of mouse embryonic stem cells into gastruloids. Nature *562*, 272-276. 10.1038/s41586-018-0578-0.
9. Veenvliet, J.V., Bolondi, A., Kretzmer, H., Haut, L., Scholze-Wittler, M., Schifferl, D., Koch, F., Guignard, L., Kumar, A.S., Pustet, M., et al. (2020). Mouse embryonic stem cells self-organize into trunk-like structures with neural tube and somites. Science *370*. 10.1126/science.aba4937.
10. Moris, N., Anlas, K., van den Brink, S.C., Alemany, A., Schroder, J., Ghimire, S., Balayo, T., van Oudenaarden, A., and Martinez Arias, A. (2020). An in vitro model of early anteroposterior organization during human development. Nature *582*, 410-415. 10.1038/s41586-020-2383-9.
11. van den Brink, S.C., and van Oudenaarden, A. (2021). 3D gastruloids: a novel frontier in stem cell-based in vitro modeling of mammalian gastrulation. Trends Cell Biol *31*, 747-759. 10.1016/j.tcb.2021.06.007.
12. Bolondi, A., Haut, L., Gassaloglu, S.I., Burton, P., Kretzmer, H., Buschow, R., Meissner, A., Herrmann, B.G., and Veenvliet, J.V. (2021). Generation of Mouse Pluripotent Stem Cell-derived Trunk-like Structures: An in vitro Model of Post-implantation Embryogenesis. Bio Protoc *11*, e4042. 10.21769/BioProtoc.4042.
13. Arias, A.M., Marikawa, Y., and Moris, N. (2022). Gastruloids: Pluripotent stem cell models of mammalian gastrulation and embryo engineering. Dev Biol *488*, 35-46. 10.1016/j.ydbio.2022.05.002.
14. Budjan, C., Liu, S., Ranga, A., Gayen, S., Pourquie, O., and Hormoz, S. (2022). Paraxial mesoderm organoids model development of human somites. Elife *11*. 10.7554/eLife.68925.
15. Sanaki-Matsumiya, M., Matsuda, M., Gritti, N., Nakaki, F., Sharpe, J., Trivedi, V., and Ebisuya, M. (2022). Periodic formation of epithelial somites from human pluripotent stem cells. Nat Commun *13*, 2325. 10.1038/s41467-022-29967-1.
16. Park, J., Hsiung, H.A., Khven, I., La Manno, G., and Lutolf, M.P. (2022). Self-organizing in vitro mouse neural tube organoids mimic embryonic development. Development *149*. 10.1242/dev.201052.
17. Tarazi, S., Aguilera-Castrejon, A., Joubran, C., Ghanem, N., Ashouokhi, S., Roncato, F., Wildschutz, E., Haddad, M., Oldak, B., Gomez-Cesar, E., et al. (2022). Post-gastrulation synthetic embryos generated ex utero from mouse naive ESCs. Cell *185*, 3290-3306 e3225. 10.1016/j.cell.2022.07.028.
18. Amadei, G., Handford, C.E., Qiu, C., De Jonghe, J., Greenfeld, H., Tran, M., Martin, B.K., Chen, D.Y., Aguilera-Castrejon, A., Hanna, J.H., et al. (2022). Embryo model completes gastrulation to neurulation and organogenesis. Nature *610*, 143-153. 10.1038/s41586-022-05246-3.
19. Lau, K.Y.C., Rubinstein, H., Gantner, C.W., Hadas, R., Amadei, G., Stelzer, Y., and Zernicka-Goetz, M. (2022). Mouse embryo model derived exclusively from embryonic stem cells undergoes neurulation and heart development. Cell Stem Cell *29*, 1445-1458 e1448. 10.1016/j.stem.2022.08.013.
20. Miao, Y., Djeffal, Y., De Simone, A., Zhu, K., Lee, J.G., Lu, Z., Silberfeld, A., Rao, J., Tarazona, O.A., Mongera, A., et al. (2023). Reconstruction and deconstruction of human somitogenesis in vitro. Nature *614*, 500-508. 10.1038/s41586-022-05655-4.
21. Yamanaka, Y., Hamidi, S., Yoshioka-Kobayashi, K., Munira, S., Sunadome, K., Zhang, Y., Kurokawa, Y., Ericsson, R., Mieda, A., Thompson, J.L., et al. (2023).

Reconstituting human somitogenesis in vitro. Nature *614*, 509-520. 10.1038/s41586-022-05649-2.
22. Hamazaki, N., Yang, W., Kubo, C.A., Qiu, C., Martin, B.K., Garge, R.K., Regalado, S.G., Nichols, E.K., Pendyala, S., Bradley, N., et al. (2024). Retinoic acid induces human gastruloids with posterior embryo-like structures. Nat Cell Biol *26*, 1790-1803. 10.1038/s41556-024-01487-8.
23. Gribaudo, S., Robert, R., van Sambeek, B., Mirdass, C., Lyubimova, A., Bouhali, K., Ferent, J., Morin, X., van Oudenaarden, A., and Nedelec, S. (2024). Self-organizing models of human trunk organogenesis recapitulate spinal cord and spine co-morphogenesis. Nat Biotechnol *42*, 1243-1253. 10.1038/s41587-023-01956-9.
24. Makwana, K., Tilley, L., Chakravarty, P., Thompson, J., Baillie-Benson, P., Rodriguez-Polo, I., and Moris, N. (2024). Modelling co-development between the somites and neural tube in human Trunk-like Structures (hTLS). bioRxiv, 2024.2012.2016.628661. 10.1101/2024.12.16.628661.
25. Rossi, G., Broguiere, N., Miyamoto, M., Boni, A., Guiet, R., Girgin, M., Kelly, R.G., Kwon, C., and Lutolf, M.P. (2021). Capturing Cardiogenesis in Gastruloids. Cell Stem Cell *28*, 230-240 e236. 10.1016/j.stem.2020.10.013.
26. Rossi, G., Giger, S., Hubscher, T., and Lutolf, M.P. (2022). Gastruloids as in vitro models of embryonic blood development with spatial and temporal resolution. Sci Rep *12*, 13380. 10.1038/s41598-022-17265-1.
27. Girgin, M.U., Broguiere, N., Mattolini, L., and Lutolf, M.P. (2021). Gastruloids generated without exogenous Wnt activation develop anterior neural tissues. Stem Cell Reports *16*, 1143-1155. 10.1016/j.stemcr.2021.03.017.
28. Girgin, M.U., Broguiere, N., Hoehnel, S., Brandenberg, N., Mercier, B., Arias, A.M., and Lutolf, M.P. (2021). Bioengineered embryoids mimic post-implantation development in vitro. Nat Commun *12*, 5140. 10.1038/s41467-021-25237-8.
29. Dias, A., Pascual-Mas, P., Torregrosa-Cortés, G., McNamara, H.M., Wehmeyer, A.E., Arnold, S.J., and Martinez Arias, A. (2025). A temporal coordination between Nodal and Wnt signalling governs the emergence of the mammalian body plan. bioRxiv, 2025.2001.2011.632562. 10.1101/2025.01.11.632562.
30. Lopez-Anguita, N., Gassaloglu, S.I., Stotzel, M., Bolondi, A., Conkar, D., Typou, M., Buschow, R., Veenvliet, J.V., and Bulut-Karslioglu, A. (2022). Hypoxia induces an early primitive streak signature, enhancing spontaneous elongation and lineage representation in gastruloids. Development *149*. 10.1242/dev.200679.
31. Aguilera-Castrejon, A., Oldak, B., Shani, T., Ghanem, N., Itzkovich, C., Slomovich, S., Tarazi, S., Bayerl, J., Chugaeva, V., Ayyash, M., et al. (2021). Ex utero mouse embryogenesis from pre-gastrulation to late organogenesis. Nature *593*, 119-124. 10.1038/s41586-021-03416-3.
32. Sakai, D., Sugawara, T., Kurokawa, T., Murakami, Y., Tomosugi, M., Masuta, H., Sakata-Haga, H., Hatta, T., and Shoji, H. (2022). Hif1alpha-dependent hypoxia signaling contributes to the survival of deep-layer neurons and cortex formation in a mouse model. Mol Brain *15*, 28. 10.1186/s13041-022-00911-0.
33. Morrison, S.J., Csete, M., Groves, A.K., Melega, W., Wold, B., and Anderson, D.J. (2000). Culture in reduced levels of oxygen promotes clonogenic sympathoadrenal differentiation by isolated neural crest stem cells. J Neurosci *20*, 7370-7376. 10.1523/JNEUROSCI.20-19-07370.2000.
34. Studer, L., Csete, M., Lee, S.H., Kabbani, N., Walikonis, J., Wold, B., and McKay, R. (2000). Enhanced proliferation, survival, and dopaminergic differentiation of CNS precursors in lowered oxygen. J Neurosci

20, 7377-7383. 10.1523/JNEUROSCI.20-19-07377.2000.
35. Villaronga Luque, A., Savill, R., López-Anguita, N., Bolondi, A., Garai, S., Gassaloglu, S.I., Poddar, A., Bulut-Karslioglu, A., and Veenvliet, J.V. (2023). Integrated Molecular-Phenotypic Profiling Reveals Metabolic Control of Morphological Variation in Stembryos. bioRxiv, 2023.2012.2004.569921. 10.1101/2023.12.04.569921.
36. Bolondi, A., Law, B.K., Kretzmer, H., Gassaloglu, S.I., Buschow, R., Riemenschneider, C., Yang, D., Walther, M., Veenvliet, J.V., Meissner, A., et al. (2024). Reconstructing axial progenitor field dynamics in mouse stem cell-derived embryoids. Dev Cell *59*, 1489-1505 e1414. 10.1016/j.devcel.2024.03.024.
37. Birey, F., Andersen, J., Makinson, C.D., Islam, S., Wei, W., Huber, N., Fan, H.C., Metzler, K.R.C., Panagiotakos, G., Thom, N., et al. (2017). Assembly of functionally integrated human forebrain spheroids. Nature *545*, 54-59. 10.1038/nature22330.
38. Xiang, Y., Tanaka, Y., Patterson, B., Kang, Y.J., Govindaiah, G., Roselaar, N., Cakir, B., Kim, K.Y., Lombroso, A.P., Hwang, S.M., et al. (2017). Fusion of Regionally Specified hPSC-Derived Organoids Models Human Brain Development and Interneuron Migration. Cell Stem Cell *21*, 383-398 e387. 10.1016/j.stem.2017.07.007.
39. Sloan, S.A., Andersen, J., Pasca, A.M., Birey, F., and Pasca, S.P. (2018). Generation and assembly of human brain region-specific three-dimensional cultures. Nat Protoc *13*, 2062-2085. 10.1038/s41596-018-0032-7.
40. Song, L., Yuan, X., Jones, Z., Griffin, K., Zhou, Y., Ma, T., and Li, Y. (2019). Assembly of Human Stem Cell-Derived Cortical Spheroids and Vascular Spheroids to Model 3-D Brain-like Tissues. Sci Rep *9*, 5977. 10.1038/s41598-019-42439-9.
41. Andersen, J., Revah, O., Miura, Y., Thom, N., Amin, N.D., Kelley, K.W., Singh, M., Chen, X., Thete, M.V., Walczak, E.M., et al. (2020). Generation of Functional Human 3D Cortico-Motor Assembloids. Cell *183*, 1913-1929 e1926. 10.1016/j.cell.2020.11.017.
42. Miura, Y., Li, M.Y., Birey, F., Ikeda, K., Revah, O., Thete, M.V., Park, J.Y., Puno, A., Lee, S.H., Porteus, M.H., and Pasca, S.P. (2020). Generation of human striatal organoids and cortico-striatal assembloids from human pluripotent stem cells. Nat Biotechnol *38*, 1421-1430. 10.1038/s41587-020-00763-w.
43. Lin, M., Hartl, K., Heuberger, J., Beccaceci, G., Berger, H., Li, H., Liu, L., Mullerke, S., Conrad, T., Heymann, F., et al. (2023). Establishment of gastrointestinal assembloids to study the interplay between epithelial crypts and their mesenchymal niche. Nat Commun *14*, 3025. 10.1038/s41467-023-38780-3.
44. Kim, J.I., Miura, Y., Li, M.Y., Revah, O., Selvaraj, S., Birey, F., Meng, X., Thete, M.V., Pavlov, S.D., Andersen, J., et al. (2024). Human assembloids reveal the consequences of CACNA1G gene variants in the thalamocortical pathway. Neuron *112*, 4048-4059 e4047. 10.1016/j.neuron.2024.09.020.
45. Grosswendt, S., Kretzmer, H., Smith, Z.D., Kumar, A.S., Hetzel, S., Wittler, L., Klages, S., Timmermann, B., Mukherji, S., and Meissner, A. (2020). Epigenetic regulator function through mouse gastrulation. Nature *584*, 102-108. 10.1038/s41586-020-2552-x.
46. Stuart, T., Butler, A., Hoffman, P., Hafemeister, C., Papalexi, E., Mauck, W.M., 3rd, Hao, Y., Stoeckius, M., Smibert, P., and Satija, R. (2019). Comprehensive Integration of Single-Cell Data. Cell *177*, 1888-1902 e1821. 10.1016/j.cell.2019.05.031.
47. Lando, D., Peet, D.J., Whelan, D.A., Gorman, J.J., and Whitelaw, M.L. (2002). Asparagine hydroxylation of the HIF

transactivation domain a hypoxic switch. Science *295*, 858-861. 10.1126/science.1068592.
48. Muz, B., de la Puente, P., Azab, F., and Azab, A.K. (2015). The role of hypoxia in cancer progression, angiogenesis, metastasis, and resistance to therapy. Hypoxia (Auckl) *3*, 83-92. 10.2147/HP.S93413.
49. Lee, P., Chandel, N.S., and Simon, M.C. (2020). Cellular adaptation to hypoxia through hypoxia inducible factors and beyond. Nat Rev Mol Cell Biol *21*, 268-283. 10.1038/s41580-020-0227-y.
50. Iyer, N.V., Kotch, L.E., Agani, F., Leung, S.W., Laughner, E., Wenger, R.H., Gassmann, M., Gearhart, J.D., Lawler, A.M., Yu, A.Y., and Semenza, G.L. (1998). Cellular and developmental control of O2 homeostasis by hypoxia-inducible factor 1 alpha. Genes Dev *12*, 149-162. 10.1101/gad.12.2.149.
51. Jia, S., and Meng, A. (2021). TGFbeta family signaling and development. Development *148*. 10.1242/dev.188490.
52. Belo, J.A., Bouwmeester, T., Leyns, L., Kertesz, N., Gallo, M., Follettie, M., and De Robertis, E.M. (1997). Cerberus-like is a secreted factor with neutralizing activity expressed in the anterior primitive endoderm of the mouse gastrula. Mech Dev *68*, 45-57. 10.1016/s0925-4773(97)00125-1.
53. Perea-Gomez, A., Vella, F.D., Shawlot, W., Oulad-Abdelghani, M., Chazaud, C., Meno, C., Pfister, V., Chen, L., Robertson, E., Hamada, H., et al. (2002). Nodal antagonists in the anterior visceral endoderm prevent the formation of multiple primitive streaks. Dev Cell *3*, 745-756. 10.1016/s1534-5807(02)00321-0.
54. Yamamoto, M., Saijoh, Y., Perea-Gomez, A., Shawlot, W., Behringer, R.R., Ang, S.L., Hamada, H., and Meno, C. (2004). Nodal antagonists regulate formation of the anteroposterior axis of the mouse embryo. Nature *428*, 387-392. 10.1038/nature02418.
55. Meyers, E.A., and Kessler, J.A. (2017). TGF-beta Family Signaling in Neural and Neuronal Differentiation, Development, and Function. Cold Spring Harb Perspect Biol *9*. 10.1101/cshperspect.a022244.
56. Bardot, E.S., and Hadjantonakis, A.K. (2020). Mouse gastrulation: Coordination of tissue patterning, specification and diversification of cell fate. Mech Dev *163*, 103617. 10.1016/j.mod.2020.103617.
57. Augsburger, A., Schuchardt, A., Hoskins, S., Dodd, J., and Butler, S. (1999). BMPs as mediators of roof plate repulsion of commissural neurons. Neuron *24*, 127-141. 10.1016/s0896-6273(00)80827-2.
58. Timmer, J.R., Wang, C., and Niswander, L. (2002). BMP signaling patterns the dorsal and intermediate neural tube via regulation of homeobox and helix-loop-helix transcription factors. Development *129*, 2459-2472. 10.1242/dev.129.10.2459.
59. Stottmann, R.W., and Klingensmith, J. (2011). Bone morphogenetic protein signaling is required in the dorsal neural folds before neurulation for the induction of spinal neural crest cells and dorsal neurons. Dev Dyn *240*, 755-765. 10.1002/dvdy.22579.
60. Bertero, A., Brown, S., Madrigal, P., Osnato, A., Ortmann, D., Yiangou, L., Kadiwala, J., Hubner, N.C., de Los Mozos, I.R., Sadee, C., et al. (2018). The SMAD2/3 interactome reveals that TGFbeta controls m(6)A mRNA methylation in pluripotency. Nature *555*, 256-259. 10.1038/nature25784.
61. Velasco, S., Kedaigle, A.J., Simmons, S.K., Nash, A., Rocha, M., Quadrato, G., Paulsen, B., Nguyen, L., Adiconis, X., Regev, A., et al. (2019). Individual brain organoids reproducibly form cell diversity of the human cerebral cortex. Nature *570*, 523-527. 10.1038/s41586-019-1289-x.
62. Rosebrock, D., Arora, S., Mutukula, N., Volkman, R., Gralinska, E., Balaskas, A.,

Aragones Hernandez, A., Buschow, R., Brandl, B., Muller, F.J., et al. (2022). Enhanced cortical neural stem cell identity through short SMAD and WNT inhibition in human cerebral organoids facilitates emergence of outer radial glial cells. Nat Cell Biol *24*, 981-995. 10.1038/s41556-022-00929-5.

63. Gribben, C., Galanakis, V., Calderwood, A., Williams, E.C., Chazarra-Gil, R., Larraz, M., Frau, C., Puengel, T., Guillot, A., Rouhani, F.J., et al. (2024). Acquisition of epithelial plasticity in human chronic liver disease. Nature *630*, 166-173. 10.1038/s41586-024-07465-2.
64. Hebert, J.M., and Fishell, G. (2008). The genetics of early telencephalon patterning: some assembly required. Nat Rev Neurosci *9*, 678-685. 10.1038/nrn2463.
65. Hettige, N.C., and Ernst, C. (2019). FOXG1 Dose in Brain Development. Front Pediatr *7*, 482. 10.3389/fped.2019.00482.
66. Kimura-Yoshida, C., Nakano, H., Okamura, D., Nakao, K., Yonemura, S., Belo, J.A., Aizawa, S., Matsui, Y., and Matsuo, I. (2005). Canonical Wnt signaling and its antagonist regulate anterior-posterior axis polarization by guiding cell migration in mouse visceral endoderm. Dev Cell *9*, 639-650. 10.1016/j.devcel.2005.09.011.
67. Kemp, C., Willems, E., Abdo, S., Lambiv, L., and Leyns, L. (2005). Expression of all Wnt genes and their secreted antagonists during mouse blastocyst and postimplantation development. Dev Dyn *233*, 1064-1075. 10.1002/dvdy.20408.
68. Hoshino, H., Shioi, G., and Aizawa, S. (2015). AVE protein expression and visceral endoderm cell behavior during anterior-posterior axis formation in mouse embryos: Asymmetry in OTX2 and DKK1 expression. Dev Biol *402*, 175-191. 10.1016/j.ydbio.2015.03.023.
69. Kim, J.W., Tchernyshyov, I., Semenza, G.L., and Dang, C.V. (2006). HIF-1-mediated expression of pyruvate dehydrogenase kinase: a metabolic switch required for cellular adaptation to hypoxia. Cell Metab *3*, 177-185. 10.1016/j.cmet.2006.02.002.
70. McMahon, S., Charbonneau, M., Grandmont, S., Richard, D.E., and Dubois, C.M. (2006). Transforming growth factor beta1 induces hypoxia-inducible factor-1 stabilization through selective inhibition of PHD2 expression. J Biol Chem *281*, 24171-24181. 10.1074/jbc.M604507200.
71. Basu, R.K., Hubchak, S., Hayashida, T., Runyan, C.E., Schumacker, P.T., and Schnaper, H.W. (2011). Interdependence of HIF-1alpha and TGF-beta/Smad3 signaling in normoxic and hypoxic renal epithelial cell collagen expression. Am J Physiol Renal Physiol *300*, F898-905. 10.1152/ajprenal.00335.2010.
72. Team, R.C. (2024). R: A Language and Environment for Statistical Computing (R Foundation for Statistical Computing).
73. Hao, Y., Stuart, T., Kowalski, M.H., Choudhary, S., Hoffman, P., Hartman, A., Srivastava, A., Molla, G., Madad, S., Fernandez-Granda, C., and Satija, R. (2023). Dictionary learning for integrative, multimodal and scalable single-cell analysis. Nature Biotechnology. 10.1038/s41587-023-01767-y.
74. Wickham, H. (2016). ggplot2: Elegant Graphics for Data Analysis (Springer-Verlag New York).

Figure S1. Hypoxia alters the conventional TLS phenotype

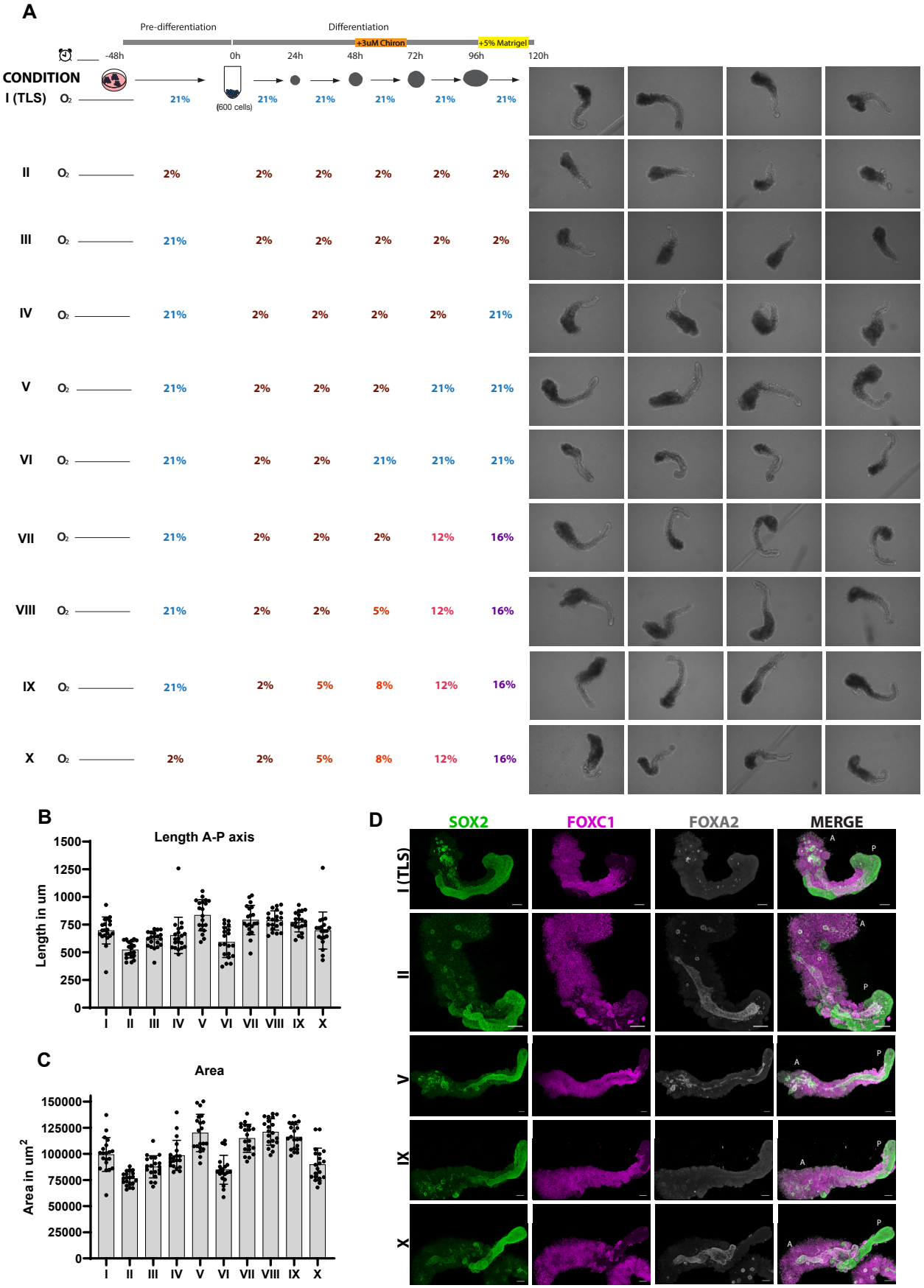

A. Schematic illustration of the experimental pipeline for TLS generation in different O_2 setups accompanied by wide-field images.
B. Graph of A-P axis length for conditions I-X. Column height and error bars indicate mean and standard deviation. Each dot represents an individual structure. Approximately 20 structures were used per condition.
C. Graph of total area per structure for conditions I-X. Column height and error bars indicate mean and standard deviation. Each dot represents an individual structure. Approximately 20 structures were used per condition.
D. IF staining of testing conditions I(Conventional TLS), II, V and IX for neural marker SOX2, somitic marker FOXC1 and endoderm marker FOXA2. A: Anterior, P: Posterior. Scale bars, 100 µm.

Figure S2. Hypoxic Assembloids recapitulate A-P patterning

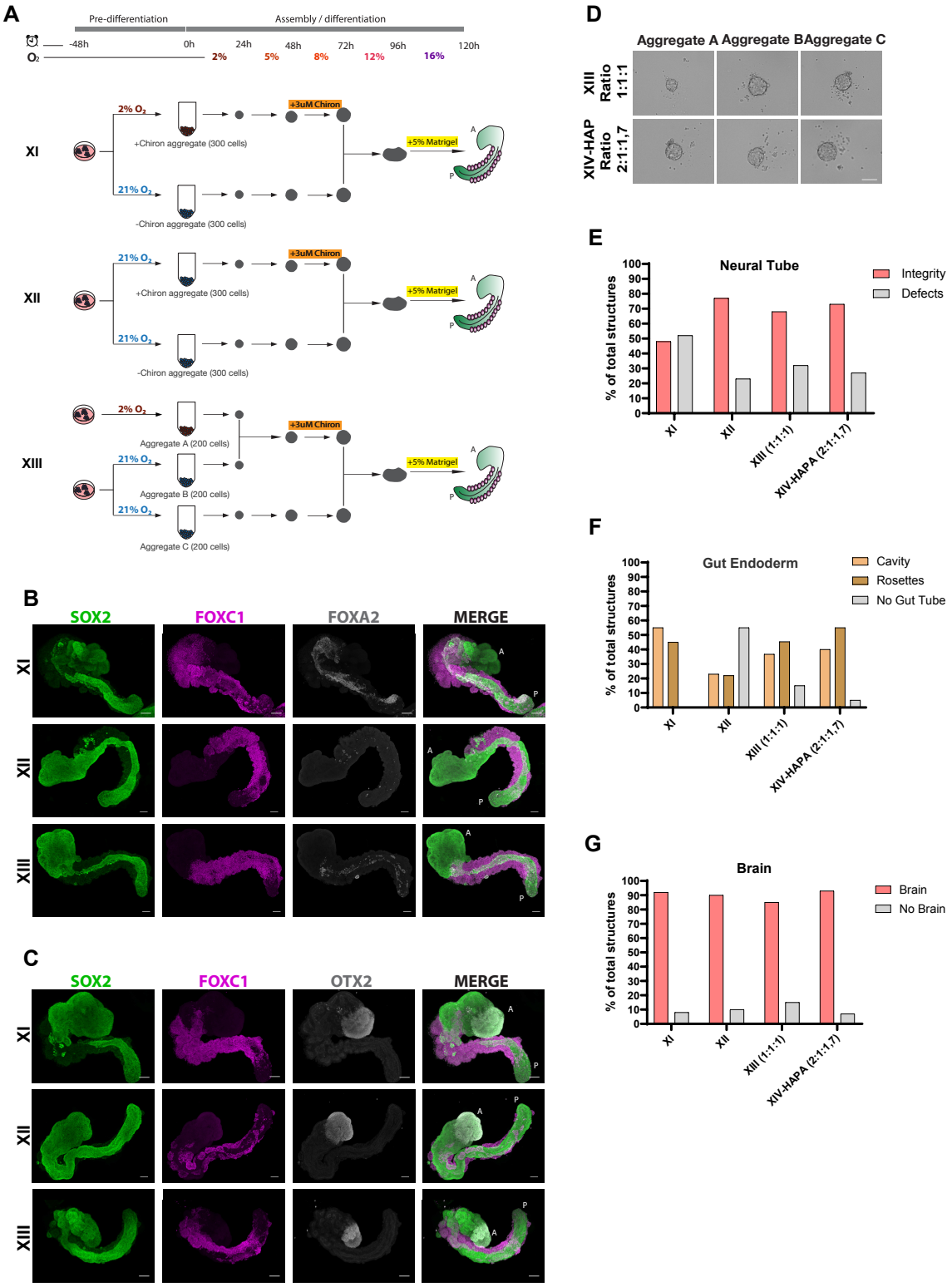

A. Schematic illustration of the experimental pipeline for Hypoxic Assembloid with WNT gradient generation.

B. IF staining of testing conditions XI, XII and XIII for neural marker SOX2, somitic marker FOXC1 and endoderm marker FOXA2. A: Anterior, P: Posterior. Scale bars, 100 µm.

C. IF staining of testing conditions XI, XII and XIII for neural marker SOX2, somitic marker FOXC1 and brain marker OTX2. A: Anterior, P: Posterior. Scale bars, 100 µm.

D. Wide-Field images of each aggregate of the triple aggregate setup at 24hrs. Two different ratios were tested in order to achieve equal aggregate size at 24hrs of the experimental pipeline. Scale bars, 100 µm. Different ratios were tried

E-G. Percentage of total structures showing neural tube integrity, gut endoderm and brain formation in conditions XI, XII, XIII and XIV (HAP-gastruloids). Column height and error bars indicate mean and standard deviation. Condition XI: For neural tube integrity 1 biological replicate was used (total number 23 structures, 11 of which had neural tube integrity). For gut endoderm formation 1 biological replicate was used (total number 11 structures, all of which formed gut endoderm). For brain formation 1 biological replicate was used (total number 12 structures, 11 of which formed brain). Condition XII: For neural tube integrity 1 biological replicate was used (total number 22 structures, 17 of which had neural tube integrity). For gut endoderm formation 1 biological replicate was used (total number 11 structures, 5 of which formed gut endoderm). For brain formation 1 biological replicate was used (total number 10 structures, all of which formed brain). Condition XIII: For neural tube integrity 4 biological replicates were used (total number 132 structures, 90 of which had neural tube integrity). For gut endoderm formation 4 biological replicates were used (total number 53 structures, 45 of which formed gut endoderm). For brain formation 4 biological replicates were used (total number 80 structures, 68 of which formed brain). Condition HAP+XAV: For neural tube integrity 11 biological replicates were used (total number 202 structures, 148 of which had neural tube integrity). For gut endoderm formation 6 biological replicates were used (total number 64 structures, 61 of which formed gut endoderm). For brain formation 15 biological replicates were used (total number 228 individual structures, 207 of which successfully formed brain).

Figure S3. Reproducibility of HAP phenotype in the KH2 ESC line

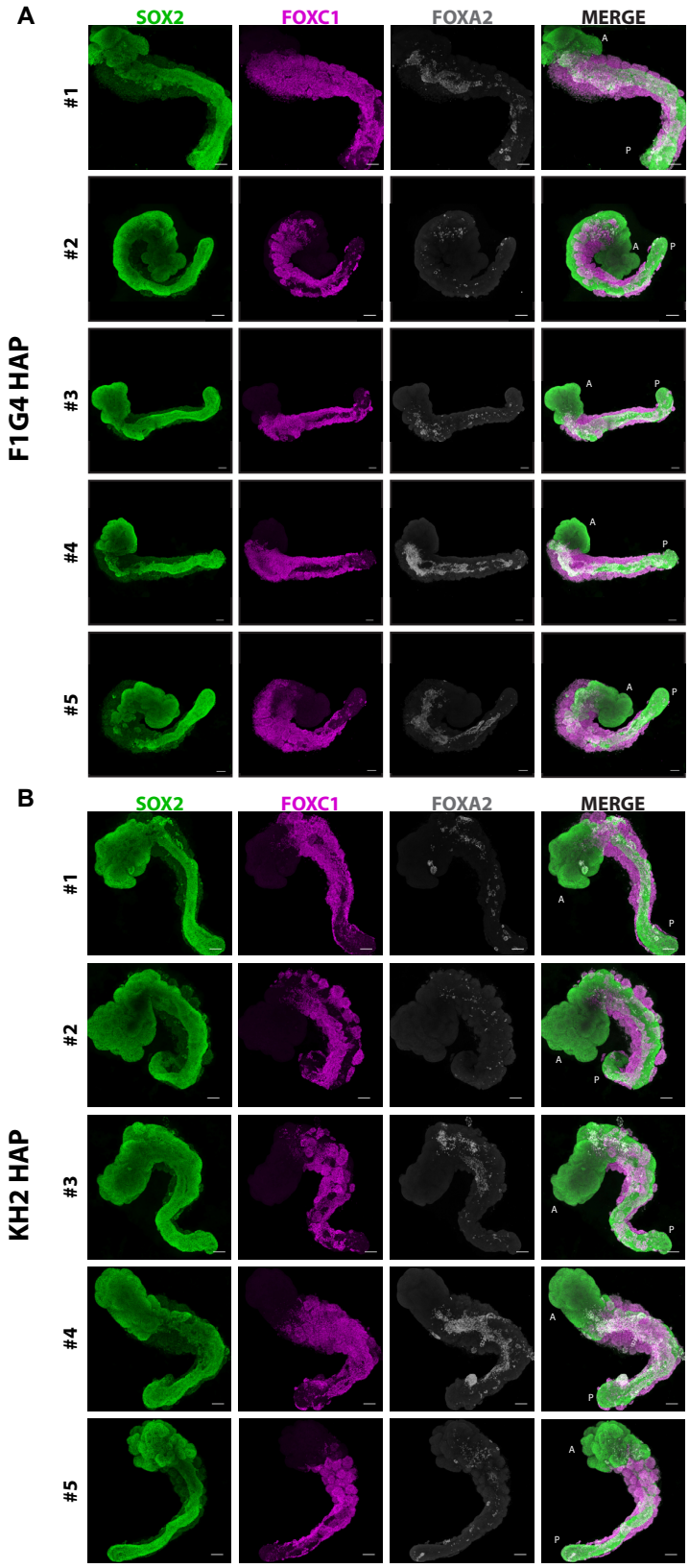

A. IF staining of F1G4-origin HAP-gastruloids for neural marker SOX2, somitic marker FOXC1 and endoderm marker FOXA2. A: Anterior, P: Posterior. Scale bars, 100 µm.

B. IF staining of KH2-origin HAP-gastruloids for neural marker SOX2, somitic marker FOXC1 and endoderm marker FOXA2. A: Anterior, P: Posterior. Scale bars, 100 µm.

Figure S4. Gene markers for cell type annotation of scRNA-seq data

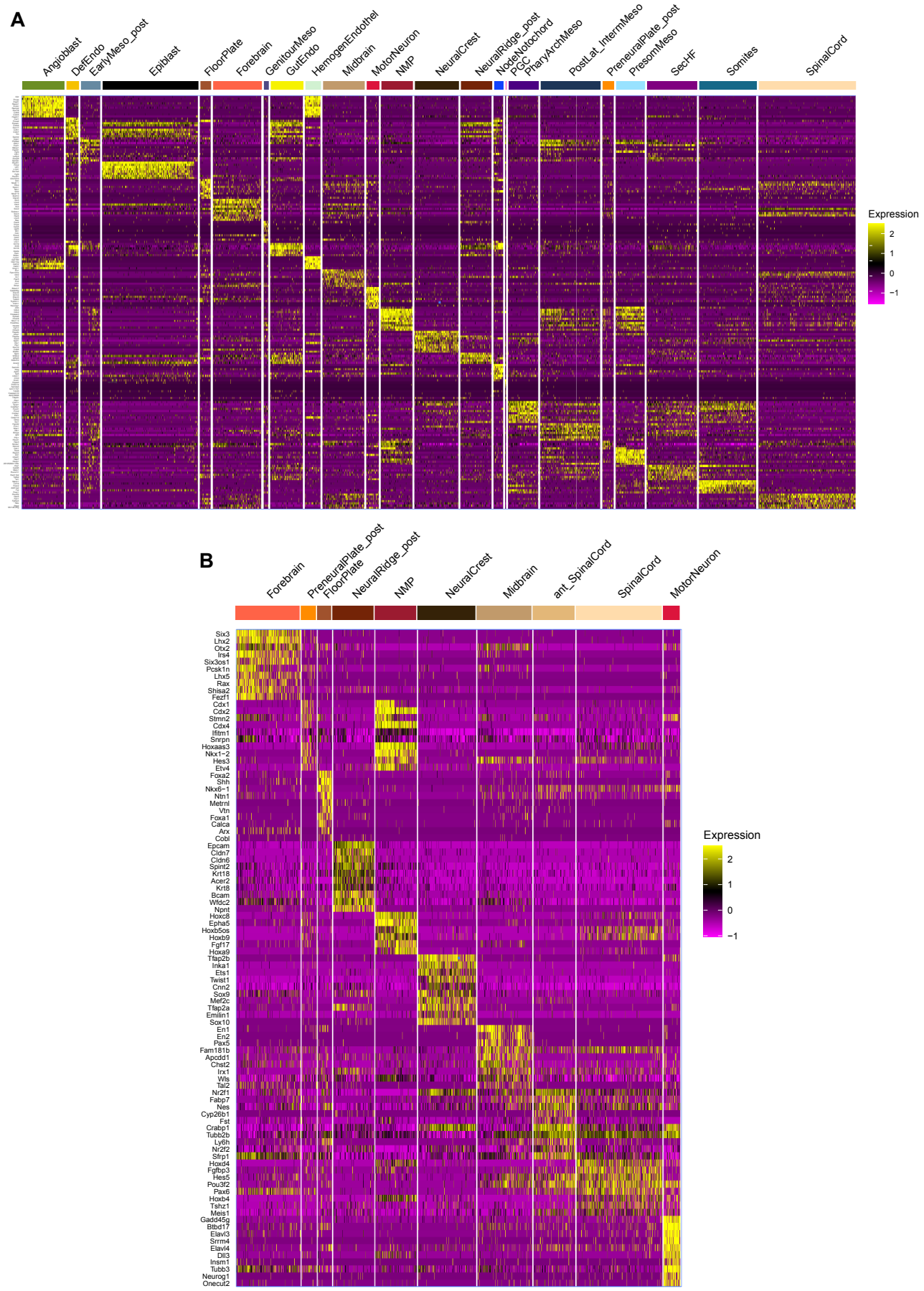

A. Heatmap showing gene markers used for cell type clustering. Color intensity reflects the scaled average expression level.
B. Heatmap showing gene markers used for neural cell type subclustering. Color intensity reflects the scaled average expression level.

Figure S5. KH2 HAPs show appropriate neural patterning along the A-P axis similar to F1G4 HAPs

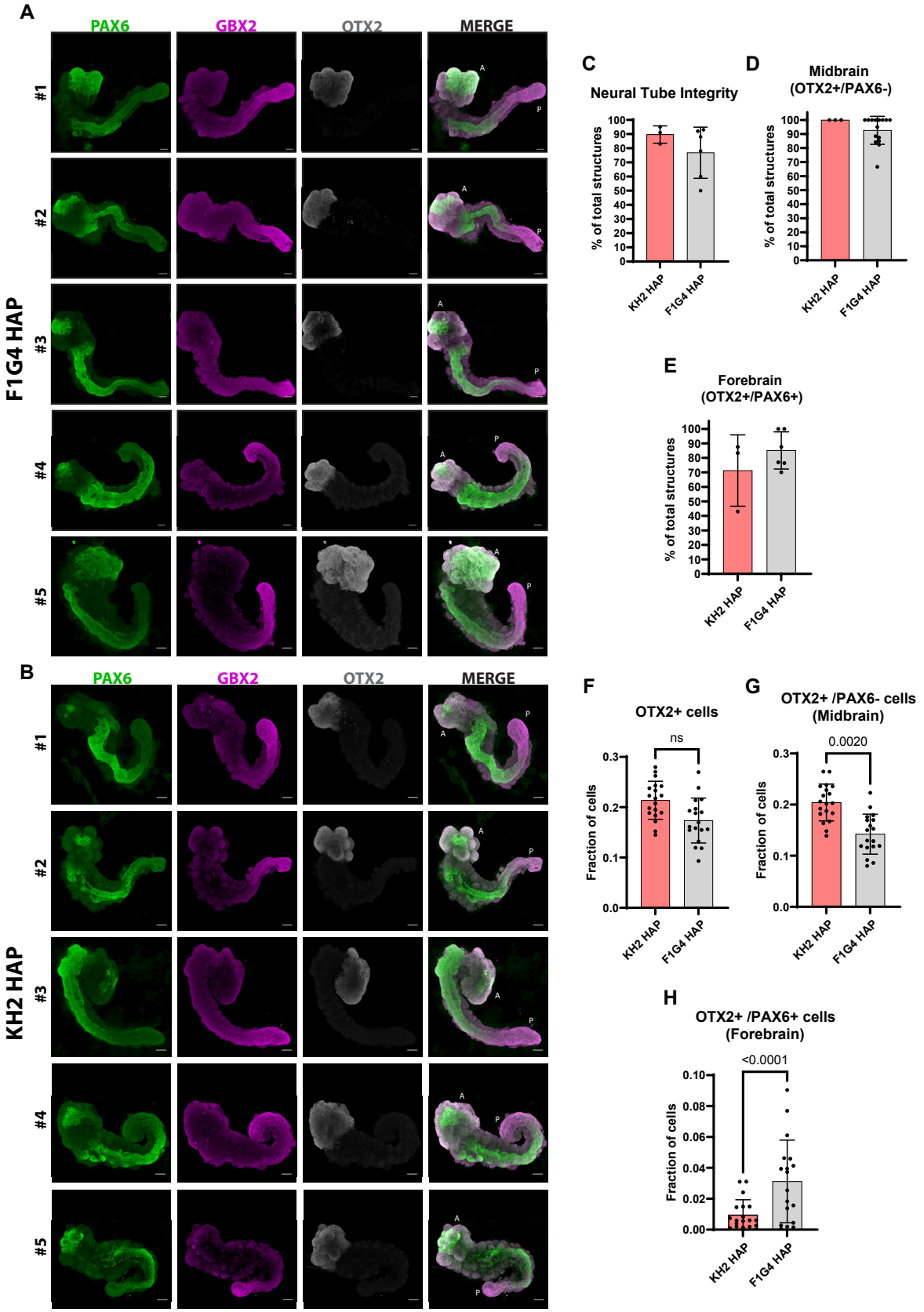

A. IF staining of F1G4-origin HAP-gastruloids for fore-/midbrain marker OTX2, hindbrain/NMP marker GBX2 and forebrain/spinal cord marker PAX6. A: Anterior, P: Posterior. Scale bars, 100 µm.

B. IF staining of KH2-origin HAP-gastruloids for fore-/midbrain marker OTX2, hindbrain/NMP marker GBX2 and forebrain/spinal cord marker PAX6. A: Anterior, P: Posterior. Scale bars, 100 µm.

C-E. Percentage of total structures per biological replicate showing midbrain and forebrain formation in F1G4 and KH2 HAP-gastruloids. Column height and error bars indicate mean and standard deviation. Each dot represents a different biological replicate. F1G4: For neural tube integrity 6 biological replicates were used (total number 600 individual structures, 461 of which had an integral neural tube along the A-P axis). For midbrain formation 15 biological replicates were used (total number 228 individual structures, 207 of which successfully formed midbrain). For forebrain formation 6 biological replicates were used (total number 67 individual structures, 56 of which successfully formed forebrain). KH2: For neural tube integrity 3 biological replicates were used (total number 54 individual structures, 48 of which had an integral neural tube along the A-P axis). For midbrain formation 3 biological replicates were used (total number 34 individual structures, all of which formed midbrain). For forebrain formation 3 biological replicates were used (total number 34 individual structures, 23 of which formed forebrain).

F-H. Fraction of cells per structure expressing OTX2+, OTX2+/PAX6- (midbrain) and OTX2+/PAX6+ (forebrain) cells in F1G4 and KH2 HAP-gastruloids. Column height and error bars indicate mean and standard deviation. Each dot represents an individual structure. F1G4: a total of 18 individual structures from 2 different biological replicates (9 structures/biological replicate) were used. KH2: a total of 19 individual structures from 2 different biological replicates (9-10 structures/biological replicate) were used. Statistical test is unpaired two-tailed t test.

Figure S6. Developmental timing and contribution of tissues derived from each aggregate

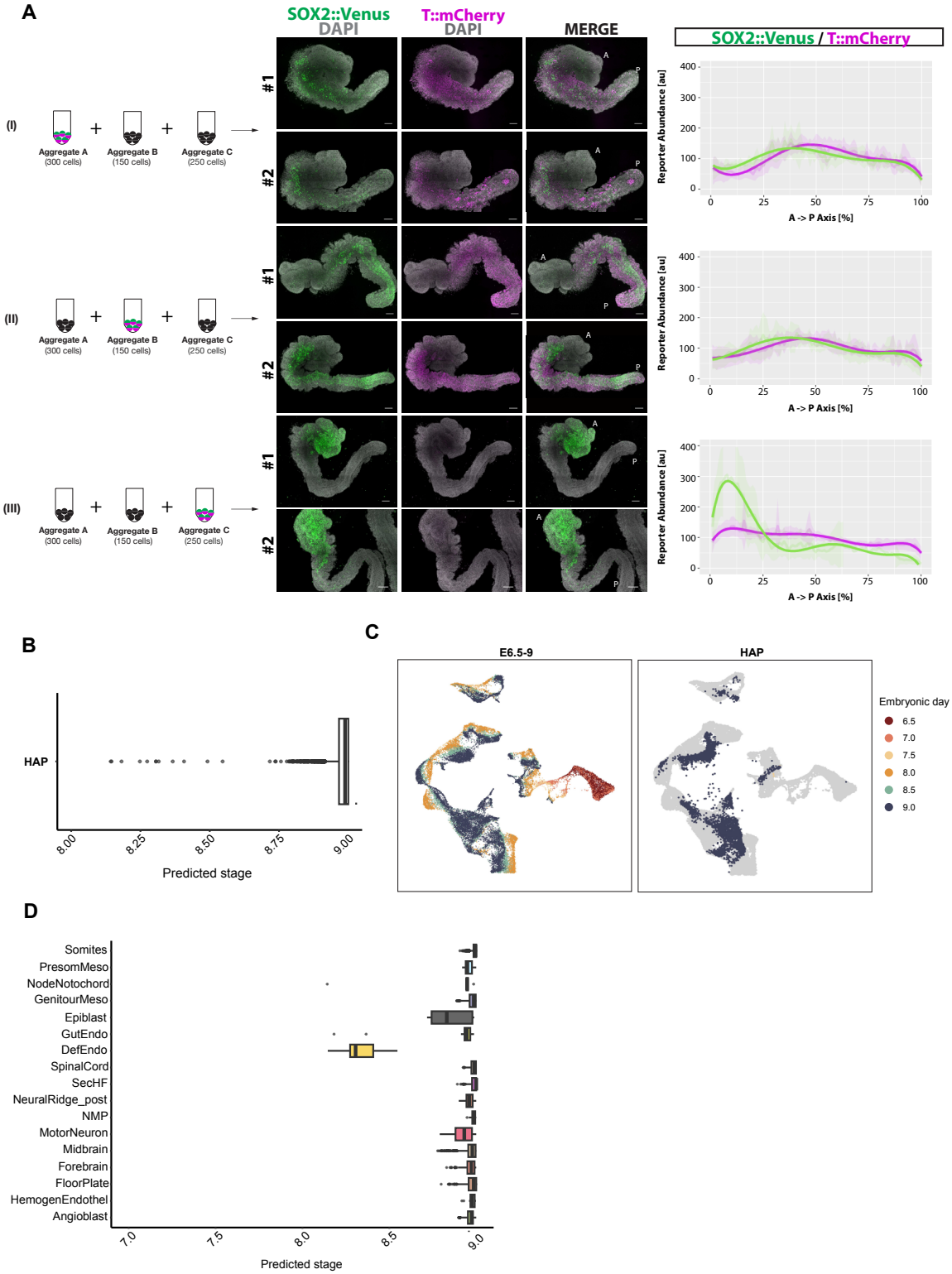

A. Contribution of each aggregate in tissue formation in HAP-gastruloids by using a dual reporter cell line for SOX2::Venus and T::mCherry. A: Anterior, P: Posterior. Scale bars, 100 µm.

B. Prediction boxplot of developmental stages that HAP-gastruloids corresponds to based on a Label Transfer-based staging analysis. Each dot represents a single cell.

C. Left, UMAP plot of mouse embryo reference scRNA-seq data stages between E6.5 to E9 [45]. Each color represents a developmental stage of the reference data. Right, UMAP plot of HAP-gastruloid scRNA-seq data. Color represents the reference based developmental stage HAP- corresponds to.

D. Prediction boxplots of developmental stages that each tissue of HAP-gastruloids correspond to based on a Label Transfer-based staging analysis. Each dot represents a single cell.

Figure S7. Normoxia impairs gut endoderm and anterior neural fate

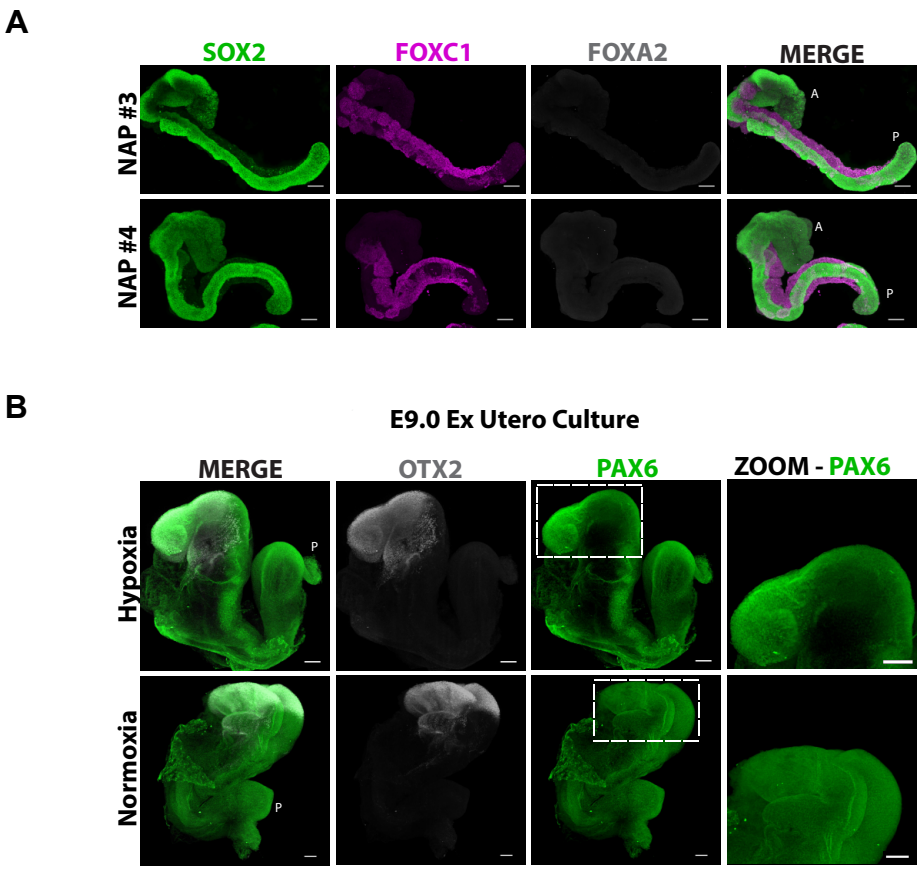

A. IF staining of NAP-gastruloids for neural marker SOX2, somitic marker FOXC1 and endoderm marker FOXA2. A: Anterior, P: Posterior. Scale bars, 100 µm.

B. IF staining of E9.0 ex utero cultured embryos for fore-/midbrain marker OTX2 and forebrain/spinal cord marker PAX6. Dash lines show areas of interest. Scale bars, 100 µm

Figure S8. Generation of the *Hif1a* KO cell line

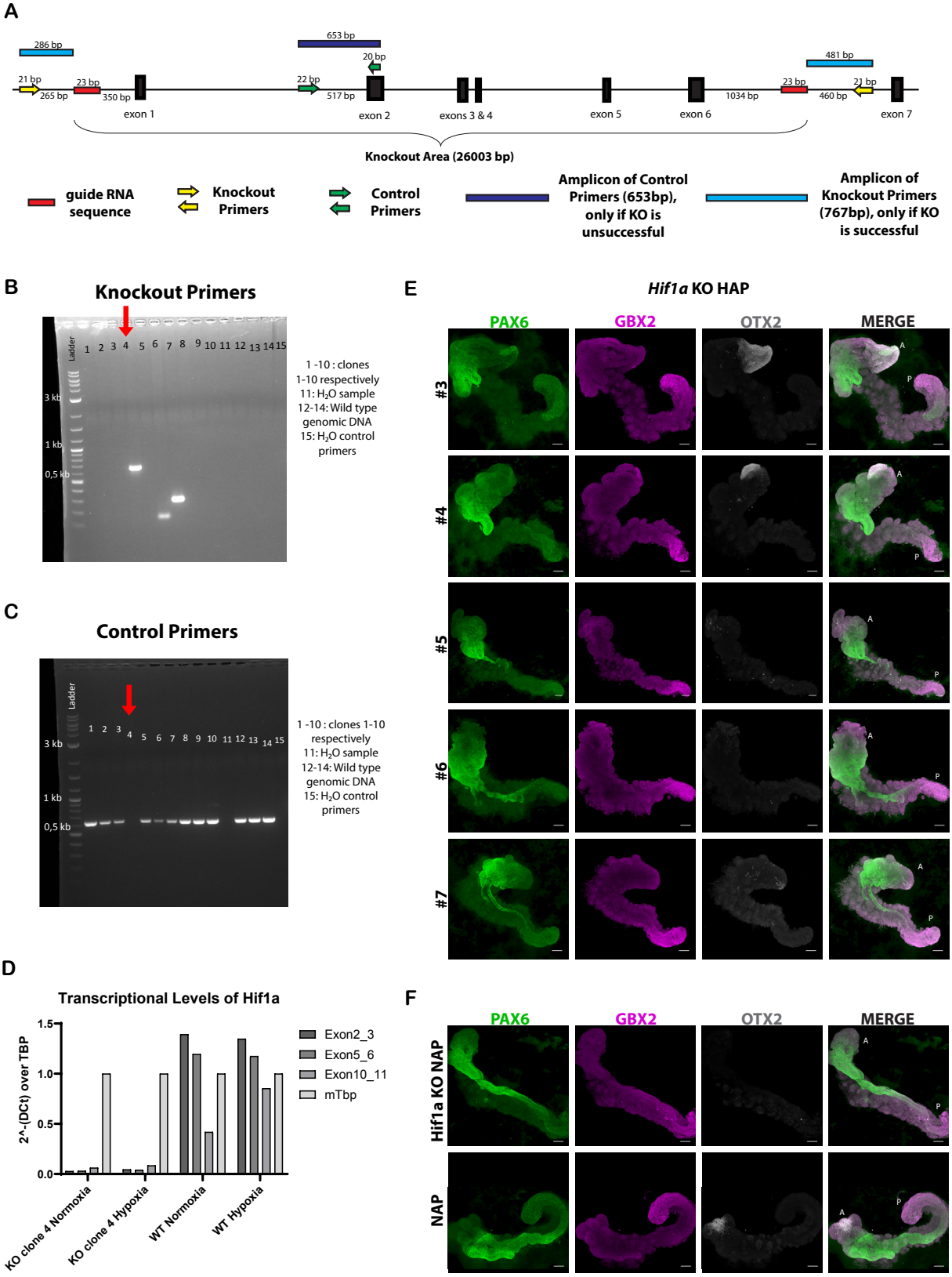

A. Schematic illustration of KO strategy in Hif1a genomic locus.
B. Genotyping PCR of *Hif1a* KO cell line with Knockout Primers.
C. Genotyping PCR of *Hif1a* KO cell line with Control Primers.
D. Real-time PCR showing the transcriptional levels of Hif1a in WT and *Hif1a* KO cells in hypoxia and normoxia. Three pairs of primers for exons 2+3, 5+6 and 10+11 were used for validation. Mouse TATA-box-binding protein (mTbp) was used as a reference target.
E. IF staining of wt and *Hif1a* KO HAP-gastruloids for fore-/midbrain marker OTX2, hindbrain/NMP marker GBX2 and forebrain/spinal cord marker PAX6. A: Anterior, P: Posterior. Scale bars, 100 µm.

F. IF staining of wt and *Hif1a* KO NAP-gastruloids for fore-/midbrain marker OTX2, hindbrain/NMP marker GBX2 and forebrain/spinal cord marker PAX6. A: Anterior, P: Posterior. Scale bars, 100 µm.

Figure S9. BMP signalling hinders forebrain formation

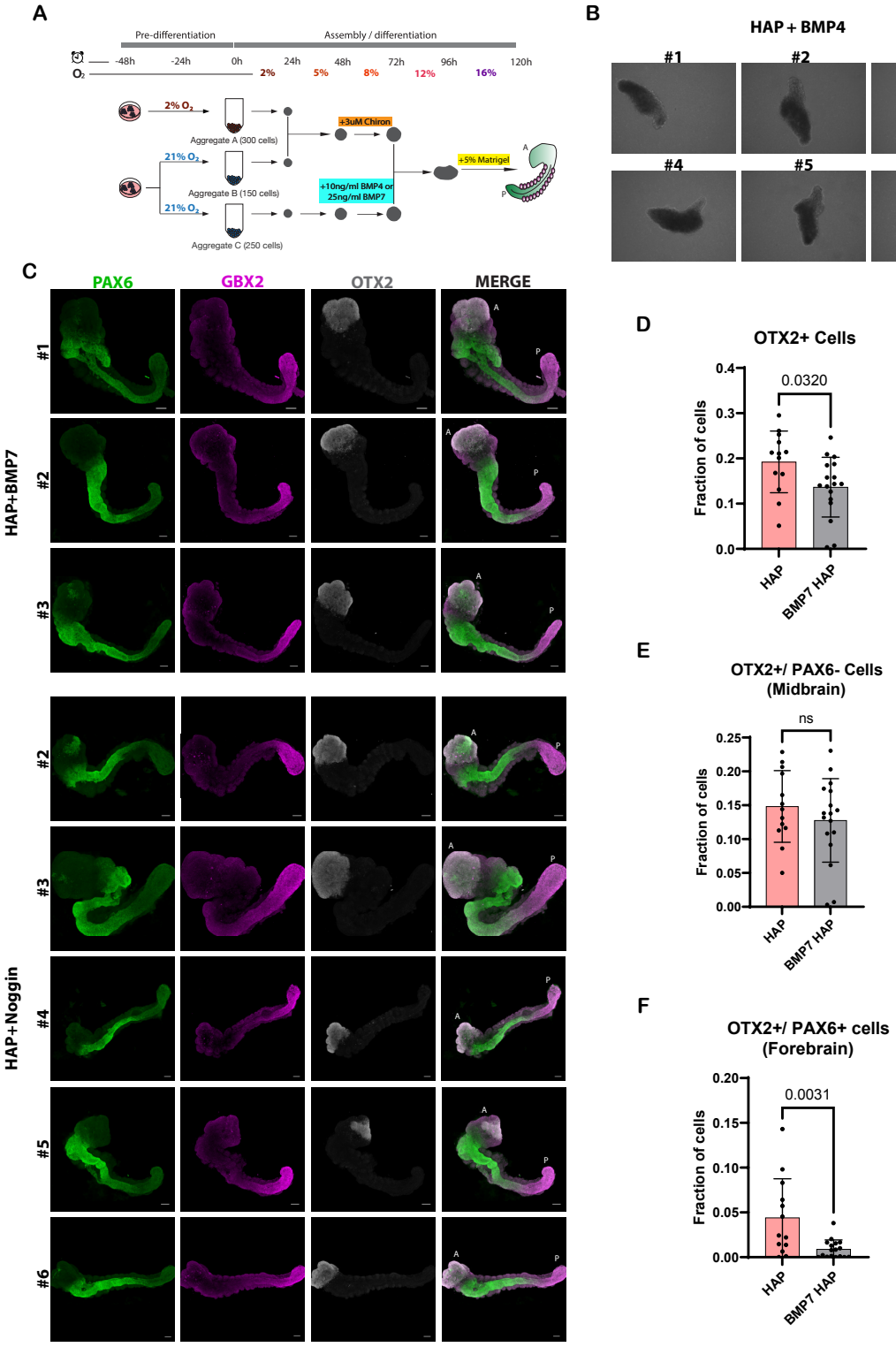

A. Schematic illustration of the experimental pipeline for treating HAP-gastruloids with BMP4 or BMP7.
B. Wide-field images of 120H HAP-gastruloids treated with BMP4.
C. IF staining of HAP-+BMP7 and HAP+Noggin for fore-/midbrain marker OTX2, hindbrain/NMP marker GBX2 and forebrain/spinal cord marker PAX6. A: Anterior, P: Posterior. Scale bars, 100 µm.

D-F. Fraction of cells per structure expressing OTX2+, OTX2+/PAX6- (midbrain) and OTX2+/PAX6+ (forebrain) cells in HAP and HAP+BMP7. Column height and error bars indicate mean and standard deviation. Each dot represents an individual structure. HAP-gastruloids: a total of 13 individual structures from 1 biological replicate were used. HAP+BMP7: a total of 17 individual structures from 2 biological replicates were used (8-9 structures/ biological replicate). Statistical test is unpaired two-tailed t test.

Figure S10. Additional stainings of HAP+TGFβ and HAP+SB

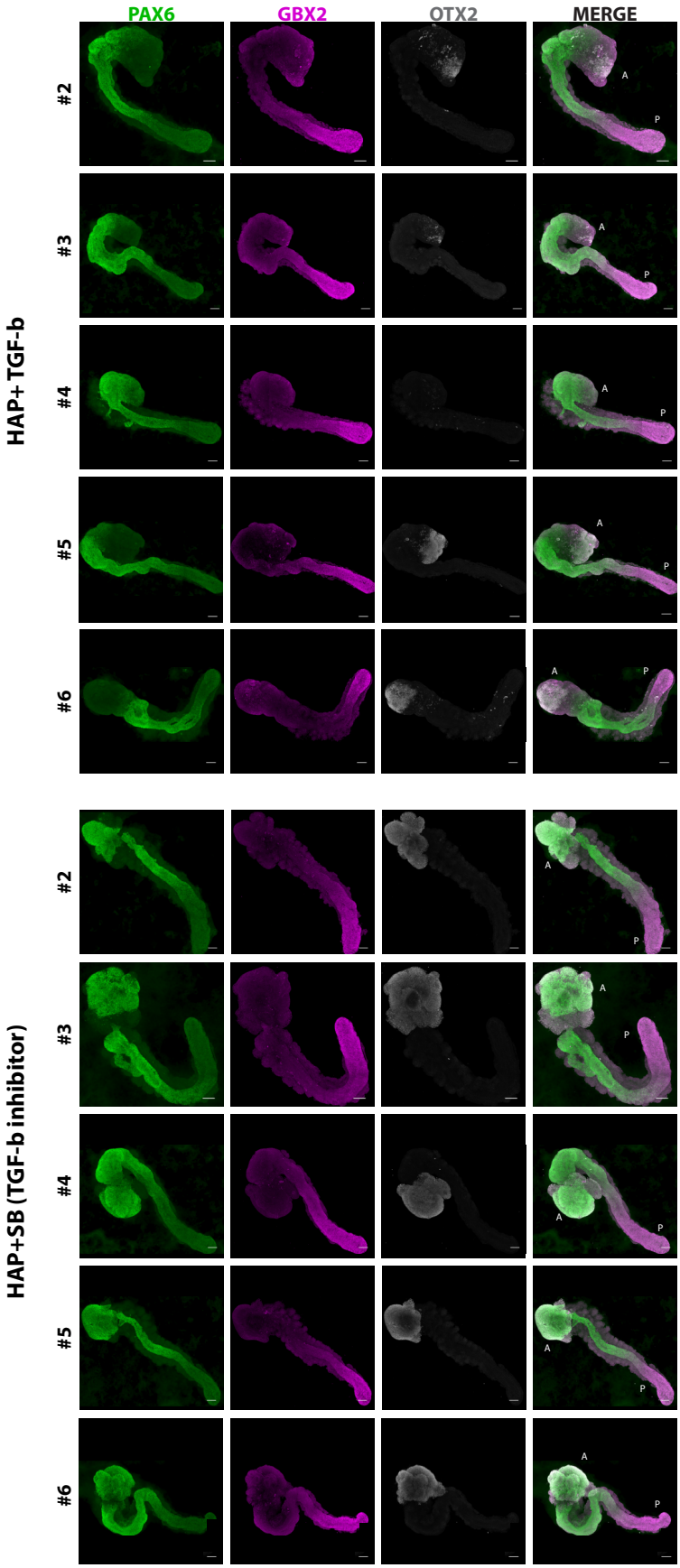

IF staining of HA+TGFβ and HAP+SB for fore-/midbrain marker OTX2, hindbrain/NMP marker GBX2 and forebrain/spinal cord marker PAX6. A: Anterior, P: Posterior. Scale bars, 100 µm.

Figure S11. WNT inhibition in HAPs induce anterior forebrain

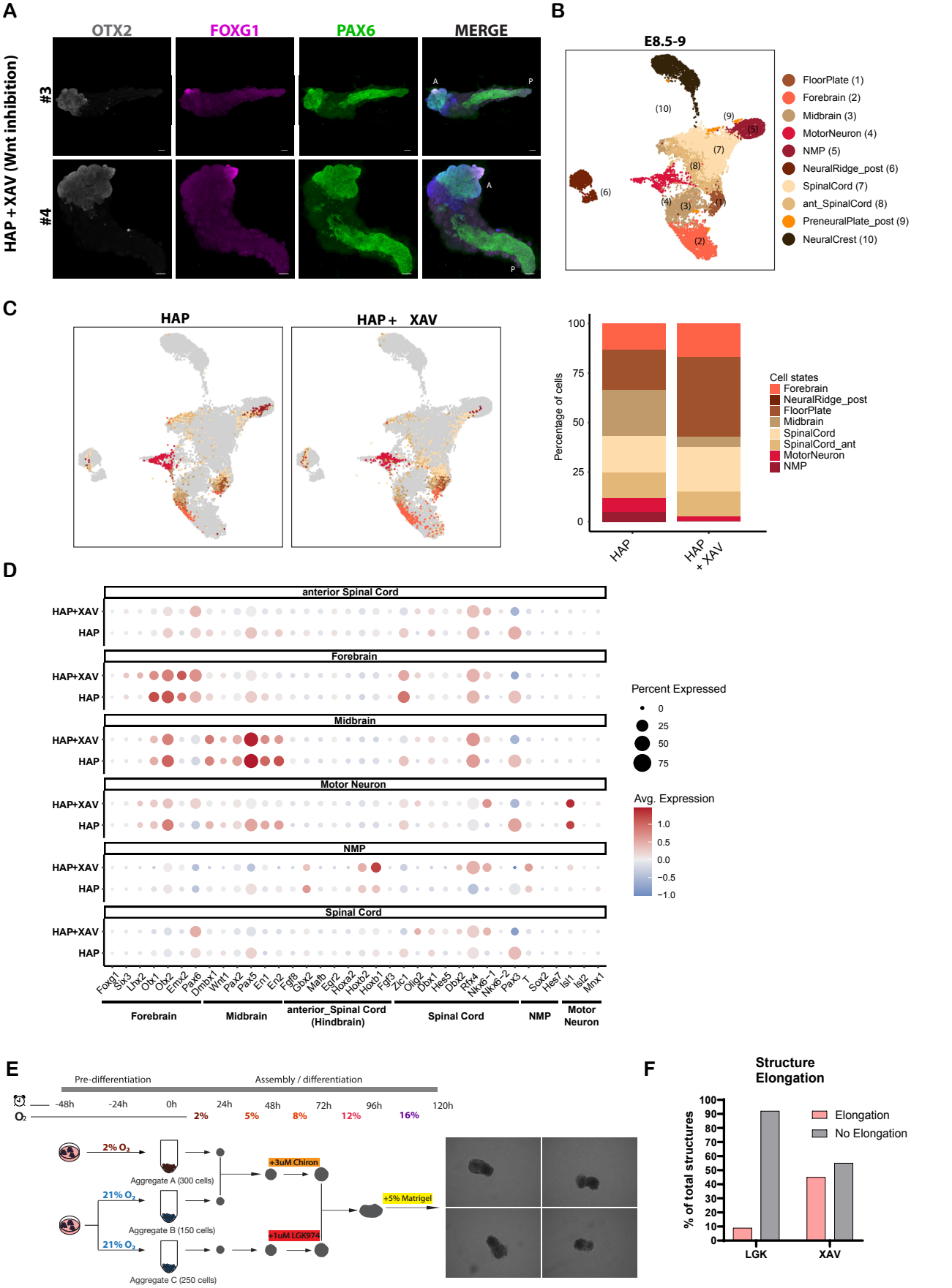

A. IF staining of HAP+XAV for fore-/midbrain marker OTX2, anterior forebrain marker FOXG1 and forebrain/spinal cord marker PAX6. A: Anterior, P: Posterior. Scale bars, 100 µm

B. Neural subclustering UMAP plot of mouse embryo reference scRNA-seq data stages between E6.5 to E9 [45]. Colors represent cell types. Cell types detected in HAP-gastruloids are shown.

C. Left, neural subclustering UMAP plot of HAP and HAP+XAV generated from scRNA-seq data. Right, stacked plots showing percentages of the indicated cell types per condition.

D. Dot plot showing the expression of neural cell type specific marker genes in HAP and HAP+ XAV. Dot size corresponds to the percentage of cells in the sample expressing the gene, while color intensity reflects the scaled average expression level.

E. Schematic illustration of the experimental pipeline for treating HAP-gastruloids with WNT inhibitor LGK974 accompanied by brightfield images.

F. Percentage of total structures showing structure elongation in XAV and LGK974 treated HAP-gastruloids. 48 total structures, 22 of which were elongated. LGK974 treatment: 46 total structures, 4 of which were elongated.

Figure S12. TGFβ and WNT inhibition do not substitute for hypoxia in NAPs

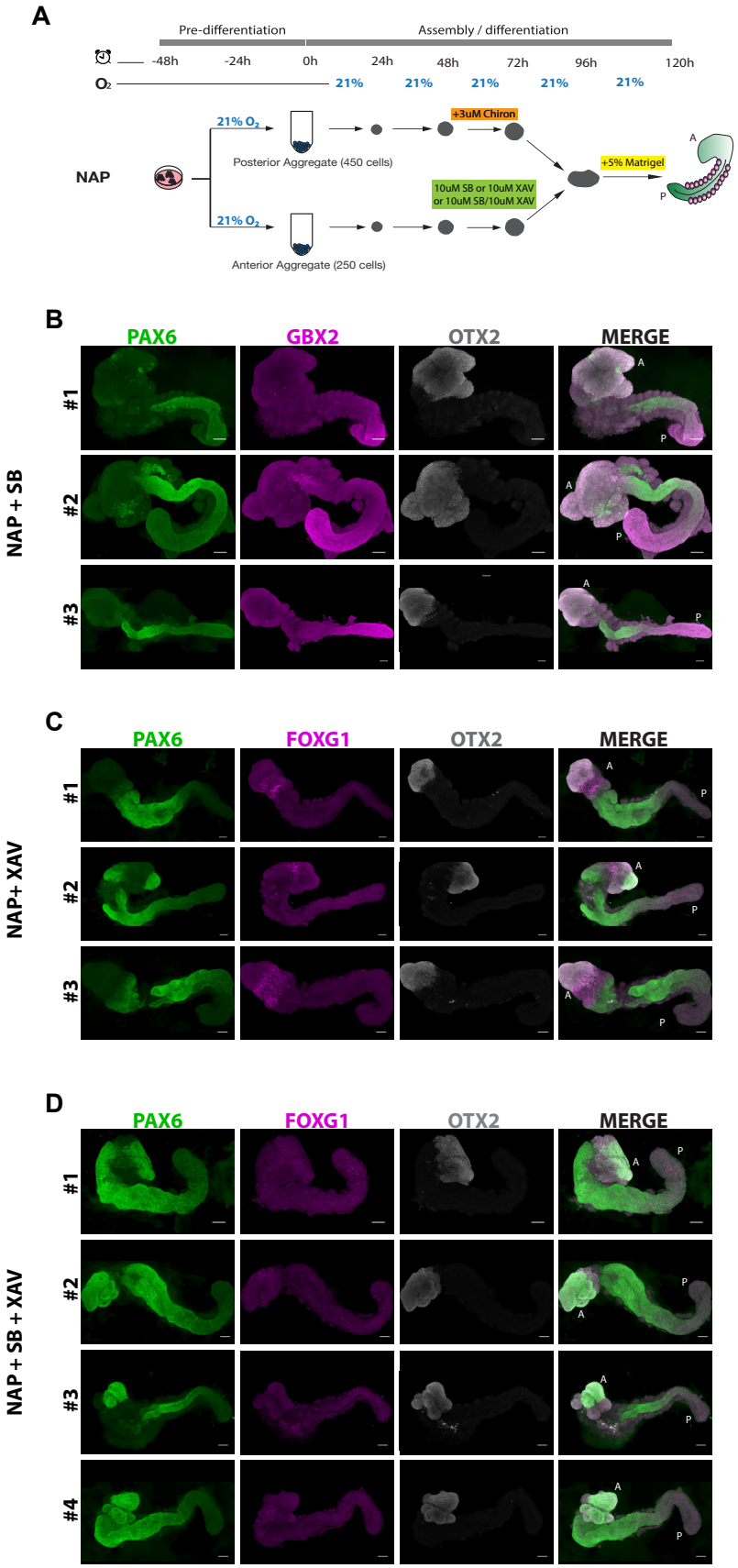

A. Schematic illustration of the experimental pipeline.
B. IF staining of NAP+SB for fore-/midbrain marker OTX2, hindbrain/NMP marker GBX2 and forebrain/spinal cord marker PAX6. A: Anterior, P: Posterior. Scale bars, 100 µm
C. IF staining of NAP+XAV for fore-/midbrain marker OTX2, anterior forebrain marker FOXG1 and forebrain/spinal cord marker PAX6. Scale bars, 100 µm
D. IF staining of HAP+SB + XAV for OTX2, FOXG1 and PAX6. Scale bars, 100 µm